2024 SOHAIL AHMED SU92-MSCHW-F22-023 FOS

Synthesis Of Copper Ferrite Nanoparticles For Carbon Dioxide Reduction

SUPERIOR UNIVERSITY

Thesis Submitted to

The Superior University Lahore

In Partial Fulfillment of the

Requirement for the Degree of

M.Phil. Chemistry

By

SOHAIL AHMED

Roll No. SU92-MSCHW-F22-023

Session: 2022-2024

Faculty of Sciences

Synthesis Of Copper Ferrite Nanoparticles For Carbon Dioxide Reduction

SUPERIOR UNIVERSITY

Thesis Submitted to

The Superior University Lahore

In Partial Fulfillment of the

Requirement for the Degree of

M.Phil. Chemistry

By

SOHAIL AHMED

Roll No. SU92-MSCHW-F22-023

Session: 2022-2024

Faculty of Sciences

Author's Declaration

I hereby state that my M.Phil. thesis titled **"Synthesis of copper ferrite nanoparticles for carbon dioxide reduction"** is my work and has not been submitted previously by me for taking any degree from this University,

The Superior University, Lahore

or anywhere else in the country/world.

At any time if my statement is found to be incorrect even after my graduation, the university has the right to withdraw my M.Phil. degree.

Name of Student: Sohail Ahmed

Date: _____

Plagiarism Undertaking

I solemnly declare that research work presented in the thesis titled **"Synthesis Of Copper Ferrite Nanoparticles For Carbon Dioxide Reduction"** is solely my research work with no significant contribution from any other person. Small contribution/help wherever taken has been duly acknowledged and that complete thesis has been written by me.

I understand the zero-tolerance policy of the HEC and University,

The Superior University, Lahore

towards plagiarism. Therefore, I as author of the above-titled thesis declare that no portion of my thesis has been plagiarized and any material used as a reference is properly referred/cited. I undertake that if I am found guilty of any formal plagiarism in the above-titled thesis, even after awarding of M.Phil. degree, the University reserves the rights to withdraw/revoke my M.Phil. degree and that HEC and the University have the right to publish my name on the HEC/University website on which names of students are placed who submitted a plagiarized thesis.

Student/Author Signature: _____

Name: Sohail Ahmed

Research Completion Certificate

This is to certify that the thesis entitled **"Synthesis of copper ferrite nanoparticles for carbon dioxide reduction"** submitted by **"Sohail Ahmed"** has been accepted towards the partial fulfillment of the requirement for M.Phil. **"Chemistry"**. The quality of the work contained in this thesis is adequate for the award of degree.

Supervisor Name: Dr. Fizza Naseem
Designation: Assistant Professor

Signature: _____

Certificate of Approval

This is to certify that the research work presented in this thesis, titled **"Synthesis of copper ferrite nanoparticles for carbon dioxide reduction"** was conducted by **"Sohail Ahmed"** under the supervision of **"Dr. Fizza Naseem"**

No part of this thesis has been submitted anywhere else for any other degree. This thesis is submitted to the Faculty of Sciences, The Superior University, Lahore in partial fulfillment of the requirements for the degree of Master of Philosophy in the field of "**Chemistry"** in Faculty of Sciences at The Superior University, Lahore.

Student Name: Sohail Ahmed Signature:_____

Examination Committee:

Session Chair: Signature:_____

a) External Examiner: Signature:_____

b) Internal Examiner: Signature:_____

c) Supervisor Name: Dr. Fizza Naseem Signature:_____

d) Name of HOD: Prof. Dr. Uqba Mehmood Signature:_____

e) Name of Dean: Prof. Dr. Mohammad Naveed Babur Signature:_____

f) Controller Examination: Dr. Muhammad Haris Signature:_____

Dedication

To

Rahmat-Ul-Lil Aalamin

Hazrat Muhammad

Sallallah-O-Alaih-E-Wasallam

And To

My dear parents, teachers, and welwishers, whose unfaltering prayers, direction, and love have served as my piller through each obstacle. Your sacrifices and belief in my ability drove me towards this achievement.

May the all-powerful bestow on you abundant blessings, vibrant health, and joyful long life.

A wholehearted thanks to my family, whose unwavering encouragement and unconditional support turned this dream into a reality.

I pay my special thanks to my parents and my paternal uncle and aunt.

I wouldn't have made it through this without you.

Acknowledgments

In the name of Allah, the Most Merciful, the Most Gracious, the Source of All Knowledge and Wisdom. We can live, learn, and prosper by the grace of Allah Almighty. I express my deepest gratitude to the Holy Prophet Muhammad (Peace Be upon Him), the world's best teacher. Without the advice and help of many people, this research could never have been finished, and I thank them sincerely. Above all, I would like to express my heartfelt gratitude to my excellent supervisor**, Dr. Fizza Naseem**, Assistant Professor Department of Chemistry, Superior University Lahore, for her exemplary guidance, unwavering patience and unremitting encouragement. She played a significant role in shaping this research through her expertise. The Department of Chemistry Program Leader Prof. **Dr. Mudassir Iqbal**, owes my sincerest thanks for his invaluable help and support. I would like to thank all of the instructors and staff for assisting me throughout my academic years. No words can express my heartfelt appreciation to my dear parents**, Mr. and Mrs. Shamsher Khan,** whose unflinching love, infinite sacrifices, and unwavering belief in me have been my greatest strength. Their prayers and encouragement helped me overcome every obstacle, allowing me to reach this goal. I would also like to thank my much-loved paternal aunt and uncle, **Mr. and Mrs. Hurmat Khan**, for their constant encouragement, kindness, and support during the course of my studies.Their guidance has been the light of hope, inspiring me towards excellence. My colleague **Miss Syeda Hajia** is particularly worth mentioning for her constant support and encouragement of my study effort. I am immensely thankful to my whole family—my strength pillars—for their love without condition. My lovely little sister, **Qamreen**, in particular, is always close to my heart. During my course, her constant spiritual encouragement and pleasant company have brought me great relief and inspiration. My experience was greatly enriched by the encouragement of my research fellows, to which I would like to thank. Lastly, I would like to thank the lab assistants for their efforts and assistance. May Allah Almighty reward all those who have worked on this effort and accept this effort as a humble service to knowledge

Sohail Ahmed

Table of Contents

Page

List of Tables

Description **Page**

List of Figures

Description **Page**

List of Abbreviations

CO_2	Carbon dioxide
UV-Vis	Ultraviolet visible spectroscopy
NH_4Cl	Ammonium chloride
$(NH_4)_2CO_3$	Diammonium carbonate
HCOOH	Formic acid
CO	Carbon monoxide
CH_4	Methane

ABSTRACT

Global efforts to find sustainable ways to convert CO_2 have been fueled by the increasing atmospheric concentration of CO_2, primarily due to modernization and increasing populations. Solar-powered photocatalytic conversion of CO_2 to useable hydrocarbons has garnered significant attention among these. The clean production of renewable fuels and mitigation of climate change are made possible by photocatalytic technologies, which replicate natural photosynthesis. However, their practical applications are still hampered by difficulties such as slow reaction kinetics, low product selectivity, and electron-hole recombination. Copper ferrite ($CuFe_2O_4$), a spinel metal oxide semiconductor, has been explored as a potential choice for photocatalytic CO_2 reduction because of its low band gap, stability, and superior redox properties. A composite of binary copper oxide doped copper ferrite (CuO-CF) was created to further boost its photocatalytic activity. This alteration leads to oxygen vacancies (OVs) and bandgap tunability, which boost CO_2 photoreduction efficiency by overcoming inherent kinetic barriers. The synthesized CuO-CF nanocomposite, which was created via an in situ co-precipitation process, showed improved electron transport capacities and better charged recombination suppression. Being exposed to UV-Vis light, the CuO-CF composite showed strong photocatalytic activity towards CO_2 reduction with methanol (CH_3OH) as the major product, using water as a sacrificial electron donor. In particular, compared to CuO or $CuFe_2O_4$ systems alone, CuO doping improved light absorption and had synergistic effects with $CuFe_2O_4$, so that the CH_3OH yield was higher 0.120 μmol g^{-1}cat h^{-1}. With a quantum efficiency of 3.5% at 267/400 nm, the binary compound demonstrated the ability to preserve interfacial charge separation and inhibit backward processes. Additionally, a pseudo-first-order model kinetic analysis confirmed the reliable and efficient conversion mechanism.

CHAPTER 1

INTRODUCTION

Particular emphasis has recently been paid to the subject of nanoparticles in a variety of sectors. The word "nano" is derived from the Greek word "nanos," meaning dwarf, and describes a size of one-billionth (10–9) of a meter [1]. Metal nanoparticles are particulate diffusions of solid units that have at least one measurement at a size range of 10–1000 nm. The most crucial feature of metal nanoparticles is their surface area to volume aspect ratio, which facilitates their facile interaction with other particles [2]. The science of nanotechnology has advanced significantly in recent years, and there are now many tested methods for producing nanoparticles with exact sizes and shapes that have been determined for specific purposes. Additionally, the number of creative uses for nanoparticles and nanomaterials is growing rapidly, and the application of effective nanomaterials has led to a better understanding of biology [3]. Previous studies have demonstrated the ability of many biological systems, such as plants and algae [4], bacteria [5], fungi [6], diatoms [7], yeast [8], and human cells [9], to convert inorganic metal ions into metal nanoparticles by using the reductive characteristics of their proteins and metabolites. The properties of macro- and micro-sized materials, which are actively employed in human health and medicine, are very different from those of nanoparticles. In addition, nanoparticles are usually classified based on their dimensionality, shape, alignment, regularity, and accumulation (Figure 1.1).

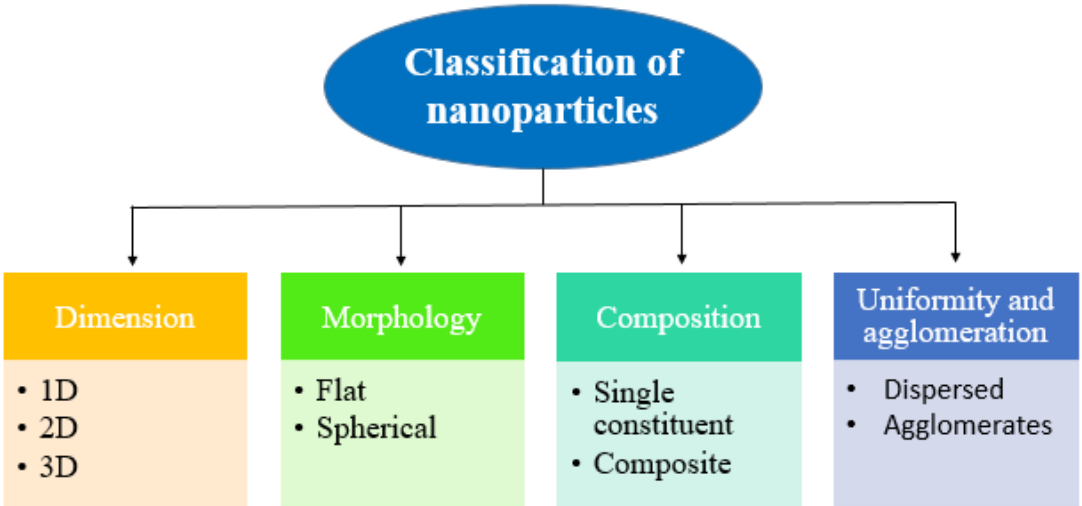

Figure 1.1 Classification of nanoparticles

Nanoparticles' morphology and structure have a significant impact on their functionality as well as their detrimental impacts on people and the environment [10]. A nanoparticle's dimensionality determines whether it is one-, two-, or three-dimensional. One-dimensional particles contain thin sheets used in electronics and sensing devices. Two-dimensional nanomaterials are composed of carbon nanotubes, which have a high adsorption capacity and stability. Three-dimensional nanoparticles contain dendrimers, quantum dots, and other components [11]. Accordingly, the morphology of nanoparticles can be classified as crystalline, spherical, or flat.

Similarly, they can exist as nanocomposites that or as separate entities. For a certain procedure or decision, engineered nanomaterials are taken into account. Metallic nanoparticles are used in a wide range of industries, including water treatment, environmental remediation/reclamation, pest management, biomedical, catalysis, and biological sensing. Metallic metal nanoparticles are usually created by decreasing their parent ion in a number of ways. There are numerous methods for creating metal nanoparticles, and the production of these particles varies according to the intended result. Figure 1.2 describes the processes used to produce metal nanoparticles.

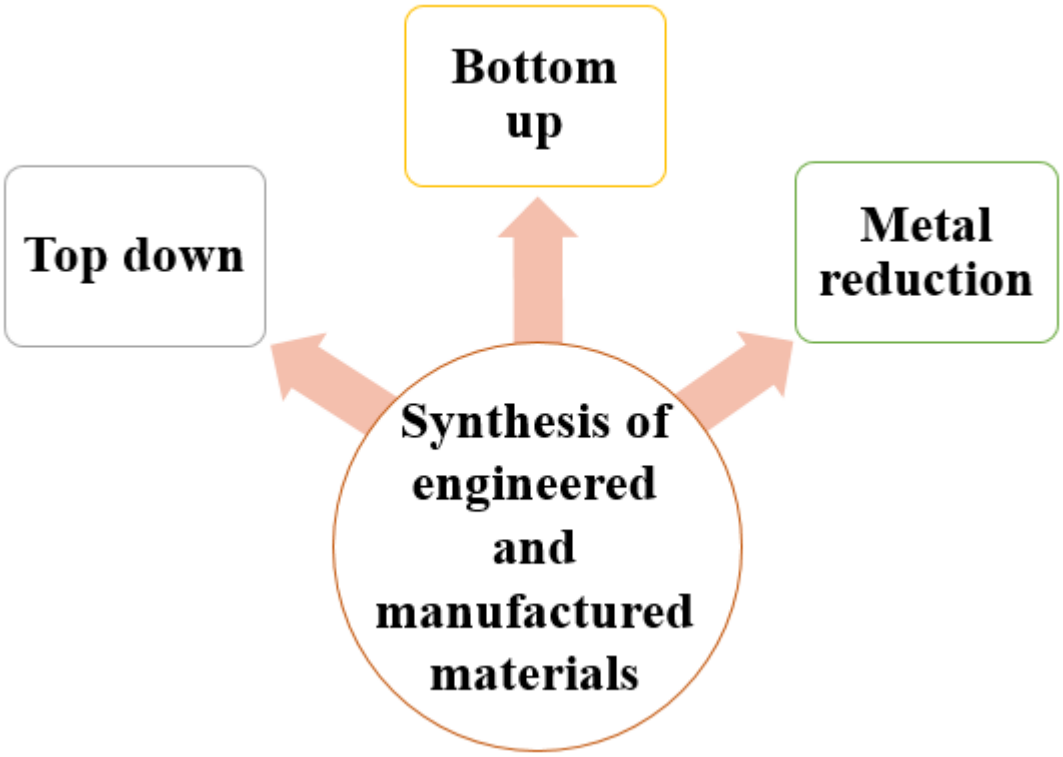

Figure 1.2 Traditional techniques for the synthesis of engineered and manufactured metal-based nanomaterials.

1.1 Copper Ferrite Nanoparticles

Several investigations have been undertaken on ferrite-based the nanomaterials, which are often defined as iron oxides with one or more metals in their structure and ferromagnetic properties. These iron oxides are classified according to their crystal structure and magnetic characteristics. The most well-known ferrites are spinel ferrites and garnet (M3Fe5O12) [12, 13], orthoferrite ($MFeO_3$) [14, 15], and hexaferrite (hexagonal crystal structure, such as $BaFe_{12}O_{19}$ and $SrFe_{12}O_{19}$) [16-18]. M stands for rare earth cations. Where A and B are metal cations situated at rectangular and octahedral sites, respectively, spinel ferrites are usually denoted by the chemical formula AB_2O_4. In reality, the product cannot be called spinel ferrite until ferric (Fe^{3+}) is included in the chemical formula.

Any metal with an oxidation temperature of +2, such as Co^{2+}, Cu^{2+}, Fe^{2+}, Mn^{2+}, Ni^{2+}, and Zn^{2+}, can be an M. The most common form of spinel ferrites is MFe_2O_4 [19-23]. Of the ferrites that were described above, spinel ferrites have garnered a lot of attention recently due to their wide variety of uses in various fields, excellent chemical and thermal stability, and superparamagnetic properties at the nanoparticle size. In contrast to other spinel ferrites, researchers used to place a lot of emphasis on magnetite (Fe_3O_4) and magnetite (γ-Fe_2O_3), that solely include oxygen as well as iron in their structure [19, 24, 25]. However, the physical properties of Fe_3O_4 nanoparticles might change based on the situation. At low pH, for example, they become considerably unstable and change into other oxides. , which alters their magnetic characteristics [26, 27].

Most of the spinel ferrites offer better physical characteristics than Fe_3O_4 NPs, such as increased surface area, improved magnetic properties, and good chemical stability [28, 29]. According to Hill and colleagues' tolerance factor equation (1), a spinel structure can only appear if the tolerance factor is approximately unity [30, 31].

$$T = \frac{1}{\sqrt{3}}\left(\frac{rA+RO}{rB+RO}\right) + \frac{1}{\sqrt{2}}\left(\frac{RO}{rB+RO}\right) \quad (1)$$

The ionic radii of the tetrahedral (A) and octahedral (B) sites are denoted by rA and rB, respectively, while RO is the radius of the oxygen ion. The placement of the +2 and +3 cations in the crystal structure of the spinel nanoparticles of ferrite (SFNPs) determines the three understood types of spinel ferrites: normal, inverse, and mixed. In normal spinel ferrite, M^{2+} ions occupy the tetrahedral sites, while Fe^{3+} ions occupy the octahedral locations. Typical examples of normal spinal ferrite are $CdFe_2O_4$ and $ZnFe_2O_4$ [32]. In an inverse spinel ferrite, the Fe^{3+} ions have a 50% ratio of tetrahedral to octahedral sites, while the M^{2+} ions only occupy the octahedral sites. Two examples are the inverse spinel ferrites $NiFe_2O_4$ and Fe_3O_4. An example of a mixed spinel ferrite is $MnFe_2O_4$, where the tetrahedral and octahedral sites are randomly occupied by both Mn^{2+} and Fe^{3+} [22, 33, 34]. On the other hand, depending on the synthesis conditions, $CuFe_2O_4$ can provide either an inverted or mixed spinel structural type [35-37]. The spinel ferrite structure is schematically represented in Figure 1.3 [38], and the inverse spinel crystal structure is depicted in Figure 1.4 [39].

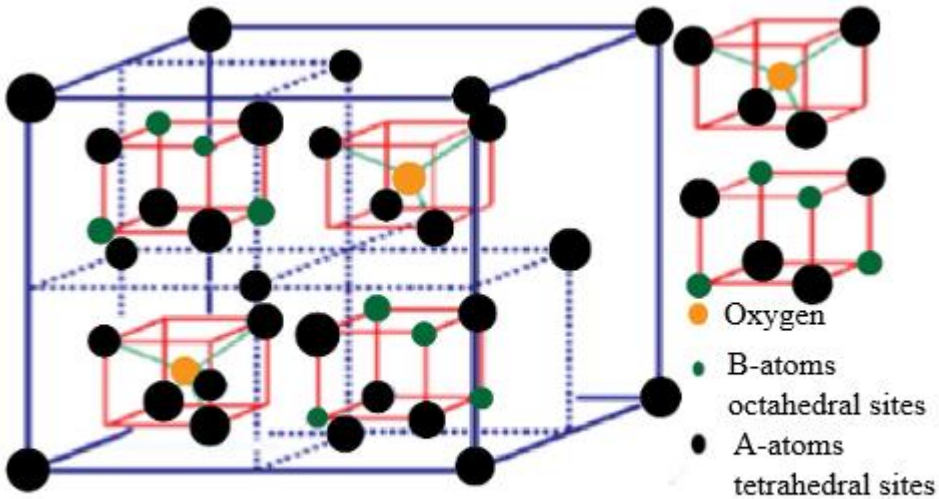

AB_2O_4 spinel: The red cubes are also contained in the black half of the unit cell

Figure 1.3 Schematic representation of the spinel ferrite.

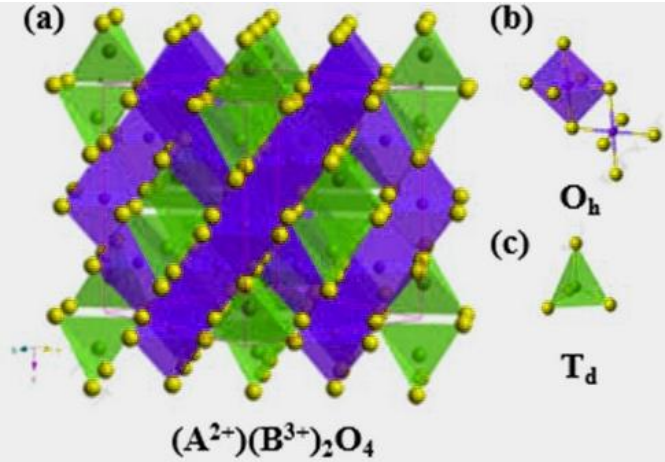

Figure 1.4 The crystal structure of an inverse spinel ferrite.

1.2 Copper Oxide Nanoparticles

Copper oxide is created by combining the elements copper and oxygen, which are located in blocks D and P of the periodic table, respectively. In a crystal, the copper ion is coordinated by four oxygen ions. Copper (Cu) and copper oxide (Cu_2O) nanoparticles have attracted a lot of attention because of copper's accessibility and significance in modern technologies [40]. The mechanical, electrical, optical, and catalytic properties of copper nanoparticles are drawing interest [41, 42]. Copper oxide is a sort of important inorganic material that is widely used in ceramics, superconductors, and catalysis. Additionally, there are electrode active materials that break down nitrous oxide with ammonia and oxidize carbon monoxide, hydrocarbons, and phenol in supercritical water. It can serve as both a catalyst and a support for catalysts [43]. While the powdered copper oxide nanoparticle is impermeable in water and soluble in diluted acid, NH_4Cl, $(NH_4)_2CO_3$, and potassium cyanide solution, it dissolves slowly in alcohols and ammonia solutions. It can change into metallic copper at high temperatures when it comes into touch with hydrogen or carbon monoxide. CuO nanoparticles can also be used as a burning rate catalyst in rocket propellant. Nano copper oxide has superior catalytic activity and selectivity above ordinary copper oxide powder. The size range of nanometer copper oxide particles is 1–100 nm. Nano CuO differs from ordinary copper oxide in a number of physical and chemical ways, including surface effect, superiority of the quantum size effect, volume effect, and macroscopic quantum tunneling effect in magnetic, optical absorption, chemical activity and thermal resistance, catalysis, and

melting point. Nano copper oxide is one of the most widely used inorganic materials and is becoming more and more well-known (Figure 1.5).

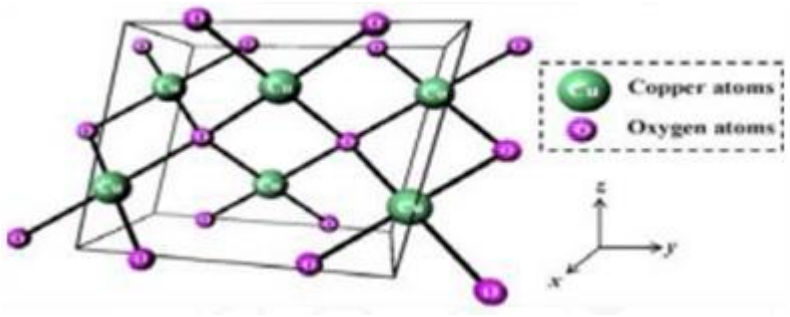

Figure 1.5 Schematic representation of a monoclinic CuO unit cell.

1.3 Copper Oxide Doped Copper Ferrite Nanocomposites

Because of their remarkable magnetic and electrical capabilities, ferrites have been the subject of much research for a wide range of applications over the past 50 years [16]. Numerous production methods, including co-precipitation [44], hydrothermal [45], sol-gel [46], auto combustion [47], micro emulsions [48], and pulsed laser ablation in liquid [49], have been used to precisely customize the properties of spinel ferrites. By using different production methods, the nano-sized spinel ferrites' size and form can be changed for usage in a range of applications [50]. Nonetheless, much research has been done to comprehend the conduction of electricity process and conductivity transitions of ferrites. It was shown that $Li_{0.5}Mn_{0.5}Fe_2O_4$ ferrite acts as a semiconducting medium that allows electromagnetic radiation to pass through it at low temperatures, but that at temperatures above 740 K, the ferrite transforms into a metallic reflector [51]. Moreover, $Ni_{1.5}Fe_{1.5}O_4$ ferrite was seen to undergo a semiconductor-metal transition [52]. Furthermore, Bhowmik and Kumar investigated the impact of pH and grain-grain boundary contribution on the semiconductor-metal like during the fabrication of $Ni_{1.5}Fe_{1.5}O_4$ spinel ferrite [52]. Furthermore, the authors investigated the low temperature semiconducting, intermediate temperature metallic-like, and high temperature semiconducting states of $Ni_{1.5}Fe_{1.5}O_4$ spinel ferrites for a range of annealing temperatures from 600 °C to 1000 °C [53]. Around 318 K, the metal-semiconductor transition was also seen in $NiFe_2O_4$ nanoparticles [54]. Ata-Allah and Kaiser also examined the changes in the conduction mechanism in the tiny nickel-manganese ferrites that were replaced with copper. They showed that when

the substitution of copper rises, the cross-over temperature at which the transition from a semiconducting state to one happens decreases [55]. Additionally, the anomalous metallic behavior seen in nanostructured cobalt ferrite at the superparamagnetic zone, which was brought on by a shift in the dominant interaction type with increasing temperature, was explained by Kannan et al. using a reverse cation migration [56].

In $Li_{0.5}Mn_{0.5}Fe_2O_{4-\delta}$, the frequency-activated conductivity transition from semiconductor to metallic state was also detected at temperatures above 800 K. To explain the metallic conductivity observed at high temperatures, they relied on the free particle-like mobility of lighter Li^+ ions amid interstitial lattices and the overlapping of electronic orbitals from neighboring ions [57]. Bhowmik and Lone also discussed the semiconductor-metal-like-semiconductor transition seen in α-$Fe_{1.6}Ga_{0.4}O_3$ between 300 and 400 K. This conductivity behavior resembled that of metal and was thought to be a phase of concealed charge conduction. They assert that the hidden charge conduction phase can emerge through the proper coupling between the electronic states and magnetic spin order, as well as the reconfiguration of the system's charge hopping mechanism [58].

1.4 Characterization Of Nanoparticles

The unique characteristics of a nanoparticle dictate its potential and uses. Utilizing a range of measuring techniques, the nanoparticles are characterized according to their size, shape, concentrations, architectures, compositions, surface areas, surface charges, surface speciations, and agglomeration [59]. Nanoparticles are categorized using microscopic methods such as electron microscopy, electron transmission, tunneling microscopy, and atomic energy microscopy (Table 1.1). Determining surface characteristics, molecular structure, chemical content, and nanoparticle size and shape may all be accomplished with the help of transmission electron microscopy and scanning electron microscopy [60].

Table 1.1 Identification of nanoparticles through characterization.

Nanoparticles	**Preparation**	**Characterization**	**Uses/Application**	**Reference**

Ferrite-based $Cs/Al/Fe_3O_4$	Precipitation technique	Scanning electron microscopy (SEM), X-ray diffraction (XRD), transmission electron microscopy (TEM), and N_2 Adsorption-desorption	High catalytic activity for biodiesel production	[61]
Activated carbon and $AC/CuFe_2O_4$ nanocatalyst	Carbonization reaction, under magnetic field with neutralization	SEM,FT-IR, XRD, EDX, TEM, and TGA	Best biodiesel yield of 95.6%	[62]

1.5 Advantages

The product can be extracted more easily and contamination can be avoided by using nano-catalysts, which are generally non-corrosive, environmentally benign, have excellent selectivity, and long lives [63]. Easy catalyst production, low cost, easy disposal, reusable qualities, and increased biofuel yield are some advantages of nano catalysts [64].

1.6 Disadvantages

Because of their distinctive properties and vast variety of applications, nanoparticles are predicted to have longer-term adverse effects on individuals and the environment. Because the nanoparticles are smaller, inadvertent inhalation by humans may induce allergic responses, lung inflammation, cardiac problems, DNA/RNA modification, and so on. [65]. Human studies show that metal-based nanoparticles affect the cardiovascular system and are harmful. Concerns should also

be raised about these immensely helpful particles' adverse impacts, especially when they are employed in large-scale operations.

1.7 CO_2 Reduction Reaction

Global energy consumption is expected to treble by 2040 [66, 67]. Fossil fuels currently provide a large portion of the energy needed, and there is mounting evidence that this limited resource is becoming scarce. Moreover, global warming has been caused by greenhouse gases (such as CO_2) released from the burning of fossil fuels [68, 69]. In order to meet energy demands while reducing CO_2 emissions, it is imperative that ecologically friendly solutions be considered. The Earth's surface currently receives more energy from the sun, a free renewable energy source, in an hour than all of humanity consumes in a year [70, 71]. As a result, solar energy can theoretically provide all of the world's energy needs. The fundamental problem, however, is that we are still unable to capture enough of this energy. The performance of photovoltaic (PV) devices has advanced recently, including notable improvements in photo conversion efficiencies [72, 73]. PV deployment has been sluggish, though, and storage has only just become a bottleneck as solar energy installations have increased. Furthermore, solar energy cannot fully replace fossil fuels due to batteries' poor energy densities as compared to chemical fuels [74, 75]. In order to achieve an environmentally friendly energy future, it is crucial to plan ahead for the possibility of efficiently storing solar energy in chemical bonds [76].

With efficient use of solar energy, "artificial photosynthesis" has been proposed as a sustainable global energy economy that would enable the photochemical conversion of anthropogenic carbon dioxide (CO_2) into useful chemical fuels (such as CO, CH_3OH, and HCOOH) [77-79]. CO_2 reduction is unquestionably a complicated reaction that is hampered by a number of kinetic and thermodynamic restrictions [80, 81]. This extremely endothermic reaction has been driven by both photo-chemical and electro-chemical mechanisms. The advantage of the photocatalytic approach is that it does not require electrode contacts and has an simplistic layout that makes device design more compact and uncomplicated. Both paths are well-liked, though, and it is difficult to predict which technology will win out in the long run. In order to carry out the chemical conversion of CO_2 into usable chemicals, the photochemical pathway uses the photon energy to start a catalytic reaction over a

photocatalyst (semiconductors). Multiple protons and electrons must progressively interact at particular catalytic sites during the intermediate phases of this intricate, multistep process [82].

The fundamental prerequisite for speeding up this complex photochemical reaction is the development of active catalysts with enhanced efficiency. Unfortunately, no one chemical has been shown to properly assist each stage of this entire procedure. This is because a single catalyst must balance two opposing requirements: on the one hand, it must span the band edge positions with respect to reduction and oxidation potentials; on the other hand, it is preferable that it possess a smaller spectrum gap for effective light harvesting and, as a result, solar conversion..

In order to attain the best possible balance between the desired characteristics, the use of composite substances as catalysts for the photocatalytic CO_2 reduction reaction is suggested. Maximum product yields from CO_2 reduction have only been reported in the literature to reach μmol scales [83, 84]. It is assumed that the poor product yields are caused by substantial recombination losses during CO_2 photocatalytic processes. To enable efficient involvement in redox reactions, photogenerated electron and hole pairs must be separated.

1.8 Thermodynamic And Kinetic Constraints

Thermodynamically, direct reduction of CO_2 is not possible (DG > 0, equations 1 & 2). This is related to the fact that CO_2 has a high C=O bond dissociation energy of » 750 $KJmol^{-1}$, making it an incredibly inert molecule [85-87]. Whether or not the system's Gibbs free energy (ΔG°) rises or falls during a chemical reaction is a measure of its spontaneity. Both DH° and TDS° are unfavorable for reducing CO_2 into other reduced products, according to the Gibbs-Helmholtz relationship [88, 89].

$$CO_2 + 2H_2O \rightarrow CH_3OH + 3/2\ O_2 \qquad \Delta G° = 689\ KJ/mol \qquad (1)$$

$$CO_2 + 2H_2O \rightarrow CH_4 + 2O_2 \qquad \Delta G° = 800KJ/mol \qquad (2)$$

$$\Delta G = \Delta H° - T\Delta S°$$

$$\Delta H° > 0 \text{ and } \Delta S° < 0$$

Here, ΔH°- enthalpy change, T- temperature, ΔS° - entropy change

In its ground state, carbon dioxide is a linear, non-polar molecule with two double bonds between carbon and oxygen that have a length of 1.17 Å [90, 91]. One electron must be transferred in order to create the CO_2 anion radical ($CO_2^{\bullet-}$), which is the first step required to decrease carbon from its most stable oxidation state (+4). A significant kinetic overvoltage (-1.90 V compared to a typical hydrogen electrode in water at pH 7) is necessary because this is kinetically unfavorable (Equation 3) [92]. The necessary structural rearrangement of the linear CO_2 molecule to the bent radical anion $CO_2^{\bullet-}$ is related to the high over potential for single electron transfer.

$$CO_2 + e^- \rightarrow CO_2^{\bullet-} \qquad E° = -1.90V \qquad (3)$$

Nevertheless, CO_2 reduction can occur through successive proton-coupled electron transfer steps with the right catalytic system, forming molecules that are thermodynamically more favorable at lower potentials [90, 93]. However, because several electrons must contribute to generate different CO_2 reduction products, reaction dynamics grow more complex.

1.9 Fundamentals Of Photocatalysis

It should be mentioned that the word "photocatalysis" is contentious when applied to thermodynamically uphill reactions [94, 95] before delving into the basics of the photocatalytic processes described in this thesis. Whether a chemical process is thermodynamically uphill or downhill depends on whether the Gibbs free energy value is positive or negative. Since light energy not only aids but also plays a crucial role in reactions with DG > 0, it is sometimes proposed that these processes be referred to as "photosynthetic" instead. On the other hand, "photocatalytic" materials use light energy to speed up a thermodynamically downhill reaction (DG < 0). However, the majority of published work still refers to the CO_2 reduction process as photocatalytic rather than photosynthetic.

Semiconductors are typically used in photocatalytic processes to increase a chemical reaction's pace without being consumed in the process [96, 97]. As previously stated, a typical photocatalyst material uses electromagnetic light (380 nm to 750 nm) to

cause chemical transformation. The three fundamental steps that it takes are as follows [97]:

- The semiconductor being used absorbs photons. Step 1 requires that the photon energy exceed the semiconductor's band gap (Ehv>= E_g).
- The production of photogenerated charge carriers (e- + h+) in the semiconductor's valence and conduction band edges (Step 2).
- Figure 1.6 illustrates how charge carriers move across the catalyst surface to take part in the next redox process (Step 4).

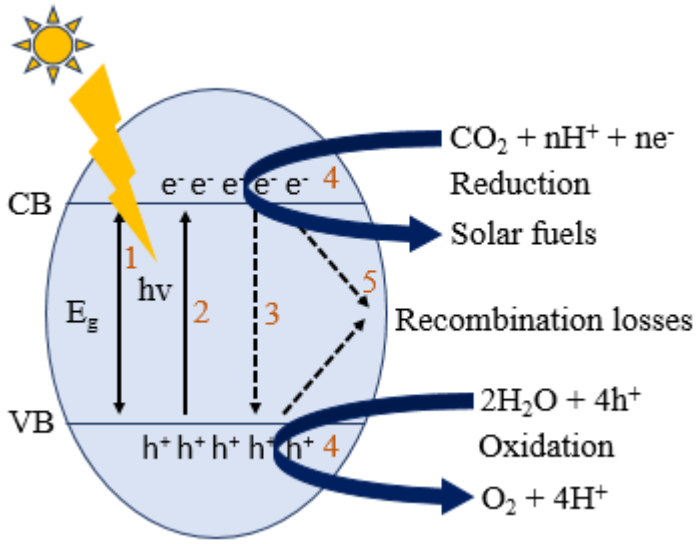

Figure 1.6 Illustrating photocatalytic CO_2 reduction with H_2O using semiconductor Photocatalyst.

Steps 1 and 2 in this case show the formation of a photogenerated charge carrier upon absorption of incident photon energy, whereas steps 3 and 5 show potential recombination losses during the process and step 4 shows the charge carrier's involvement in a redox reaction.

The photogenerated electron-hole pair can either recombine and release the excitation energy through lattice vibrational modes (Step 3) or it can move to the catalyst's surface (Step 4 in Figure 1.6) and participate in redox reactions at the corresponding redox sites [98, 99]. When migrating to redox sites, electron-hole (e^- + h^+) pair recombination can take place in the bulk as well as on the surface. It is possible for photogenerated charge carriers to recombine with their opposite charge counterparts that are trapped on the surface (surface recombination 3), or two carriers can recombine in the semiconductor's bulk (volume recombination 5) [100,

101]. Charge carriers that are successful in moving to the catalyst surface contend with potential recombination events along the way.
Therefore, the goal of this field's research is to reduce this recombination and extend the excited state lifetime of semiconducting materials.

The amount of electrons produced and, in turn, the number that make it to the reduction site determine the product production in the context of CO_2 photoreduction (Step 4 illustrated in Figure 1.6). Proton-coupled electron transfer, as previously stated, helps lower the high activation barriers for CO_2 reduction (Equation 1 vs. Equation 2). The reducing agent (such as H_2O) and reaction medium determine the proton's source. Here, a variety of multiple proton-coupled electron transfer processes can produce a range of CO_2 reduction products, with the number of electrons involved determining the product's selectivity [102, 103]. The potential byproducts of photocatalytic CO_2 reduction are listed below, along with the appropriate redox potentials (vs. NHE in water (pH-7)).

$$CO_2 + e^- \rightarrow CO_2^- \qquad E° = -1.90 \qquad (1)$$

$$CO_2 + 2e^- + 2H^+ \rightarrow HCOOH \qquad E° = -0.61 \qquad (2)$$

$$CO_2 + 2e^- + 2H^+ \rightarrow CO + H_2O \qquad E° = -0.53 \qquad (3)$$

$$CO_2 + 4e^- + 4H^+ \rightarrow HCHO + H_2O \qquad E° = -0.48 \qquad (4)$$

$$CO_2 + 6e^- + 6H^+ \rightarrow CH_3OH + H_2O \qquad E° = -0.38 \qquad (5)$$

Because they can be utilized directly as fuels, researchers are more interested in getting reaction products in higher reduction states, such methanol or methane, out of all the potential reduction products. But other products, including carbon monoxide and formic acid, are still just as valuable as feedstocks for the pharmaceutical industry.
In addition to directing reactions toward the intended products, this tactic lowers the photocatalyst's rate of electron-hole recombination, which raises quantum efficiency. Metal oxide-based photocatalysts, including TiO_2, $SrTiO_3$, CuO-Cu_2O, Co_3O_4, and $Cu_3Nb_2O_8$, have been extensively researched for CO_2 reduction. As photocathodes, P-type metal oxides are essential for photo-electrochemical CO_2 reduction. Since

these characteristics improve the efficiency of visible light absorption, catalysts with low band gaps, strong electron conductivity, and exceptional stability are preferred [104, 105]. $CuFe_2O_4$ with TiO_2 has attracted interest among metal oxide photocatalysts because of its electron conduction characteristics and inverse spinel arrangement. $CuFe_2O_4$ is synthesized using the sol-gel process and has a greater surface-to-volume ratio, good homogeneity, and crystallites that are submicron in size [106].

The primary objective of the current study is to assess the photo-electrochemical characteristics of $CuFe_2O_4$ for CO_2 reduction. Applications for $CuFe_2O_4$ nanoparticles have been identified in a variety of sectors, demonstrating their adaptability and versatility. Among their many uses, they have been used as anode materials in lithium-ion rechargeable batteries, in magnetic resonance imaging, as photocatalysts for the evolution of hydrogen driven by visible light, in energy storage materials, as catalysts in nanomedicine for the treatment of breast cancer, as facilitated coupling reactions, as CO_2 reduction catalysts, as photoanodes for solar water oxidation, as support for enzyme immobilization, and as photocatalysts [107, 108]. Despite a long list of intriguing publications about the synthesis of $CuFe_2O_4$ nanoparticles, their size and shape changes, and their application in the purification of water [109], there is a dearth of in-depth research on copper ferrite nanoparticles for CO_2 reduction because of our incomplete knowledge of their catalytic efficiency and mechanistic insights in CO_2 conversion processes.

More research is needed into the catalytic activity of copper ferrite nanoparticles for CO2 reduction procedures, such as the reduction of CO2 to helpful fuels. To maximize the effectiveness of these nanoparticles, it is also crucial to understand how selective they are toward particular substances. A comprehensive study of the chemical processes involved in the CO2 reduction process using copper ferrite nanoparticles is also necessary to develop more potent catalysts. This will help with our comprehension of detailed molecular processes.

Producing CuFe2O4 nanoparticles using a single-step production process is the primary goal of the current study. Examining copper iron oxide as a photocatalyst for CO2 reduction is a comprehensive and forward-thinking approach to address pressing environmental problems. By combining novel materials, synthesis techniques, and photocatalytic methodologies, researchers expect to contribute to the

development of sustainable and effective strategies for improving sustainable fuels and decreasing climate change.

.

1.10 Creating Efficient CuO-$CuFe_2O_4$ For Industrial And Environmental Uses

The goal of the thesis is to create exceptional performance CuO-$CuFe_2O_4$ suitable for a variety of industrial and environmental uses by optimizing production processes and carefully analyzing the substance. These applications include energy conversion and storage, sensing techniques, composite materials, and protective coatings that capitalize on CuO-$CuFe_2O_4$'s excellent electrical conductivity, hardness, and chemical stability.

The "Fabrication and Characterization of copper oxide doped copper ferrite nanoparticles (CuO-$CuFe_2O_4$) for Photocatalytic Activity" thesis addresses significant topics in environmental sustainability and materials science. The study intends to aid in the creation of innovative CO_2 reduction strategies and the integration of renewable energy sources into industrial processes by enhancing the synthesis, characterization, and application of CuO-$CuFe_2O_4$. The expected findings advance our understanding of copper-based materials and open the door to their practical use in addressing global environmental and energy issues.

AIMS AND OBJECTIVES

The aim of this research work is to:

- Synthesize $CuFe_2O_4$ nanoparticles (NPs) by sol gel method.
- Characterize $CuFe_2O_4$ nanoparticles (NPs) by XRD, FTIR and UV-visible spectroscopy.
- Enhance $CuFe_2O_4$ NPs' surface area and size by using surfactant.
- Optimize the physical parameters such as temperature and pH efficiently reduce CO_2 into beneficial products with enhanced efficiency and selectivity.

CHAPTER 2

LITERATURE REVIEW

2.1 Copper Oxide Nanoparticles

Nanoparticles, also known as NPs, are materials or particles that have one or more dimensions in the nanoscale (1–100 nm). Because we may alter their physical and chemical properties to suit our requirements and applications, they are widely used in both industries and healthcare. NPs fall into one of two distinct groups: inorganic (which includes metals, metal oxides, and quantum dots) or organic (which includes liposomes as dendrimers, and carbon-based NPs). One of the most popular kinds of metal oxide nanoparticles is copper oxide (CuO). They are more resilient, ductile, and electrically conductive because to their enhanced superconductivity, photovoltaic, and other special physicochemical characteristics. Because of these properties, they are widely used in paints, textiles, gas, batteries, semiconductors, and other biological devices. By 2025, it is anticipated that 1600 tons of copper-based nanomaterials would have been created, with a projected market value of over $150 million in 2022. Given their extensive use, further investigation into the potential harm that CuO NPs may cause to biological systems is also necessary. The assessment of NPs in the environment is currently limited due to the difficulties in analytical characterization and quantification. Although Cu has been discovered in soil, nothing is known about metal oxide nanoparticles (NPs) in aquatic settings. (Murugesan Srimathi et al., 2025) [110].

2.2 The Role Of Surfactants

There are several approaches to obtain copper oxide nanoparticles in different sizes and forms. The synthesis methods covered in the literature include thermal decomposition, calcination, pyrolysis, sonochemistry, electrochemistry, colloid formation, microwave irradiation, precipitation, reduction, reverse micelles, sol–gel method, formed themselves methods, and biosynthesis using plant extracts. A well-known oxidation-reduction method that employs a reducing agent to lower copper ions in an aqueous medium has been developed in addition to these methods. Moreover, the precipitation process is very attractive due to its simplicity. On the other hand, surfactants are essential for the production of nanoparticles.

They control the size and shape of particles and prevent them from clumping together. Dispersant molecules are expected to be adsorbed on specific crystal planes, causing the crystal structure to develop anisotropically. Furthermore, surfactant facilitates nucleation and development by lowering the interfacial energy between the solution and the nanoparticles. Depending on the surfactant used, the shape of nanoparticles can be regulated by the selective binding of ligands to particular crystal facets. During colloidal synthesis, the nanoparticles' ability to self-assemble into an ordered structure is made possible by their interaction with ligands.

Copper oxide nanoparticles have been synthesized using a variety of dispersants, such as cetyl trimethyl ammonium bromide (CTAB), ethylene glycol, polyacrylamide (PAM), poly(ethylene glycol) (PEG), polyoxyethylated lauryl ether surfactant (Brij 30), poly(vinylpyrrolidone) (PVP), sodium dodecyl benzene sulfonate (SDBS), sodium dodecyl sulfate (SDS), sodium polyacrylate, Triton X-100, and others (Guzman, Maribel, et al. (2021)) [111].

2.3 The Nanoparticles Of Copperferrite

Ferrites, mainly complex oxides containing ferric ions, are classified as magnetic materials due to their ferrimagnetic activity. Ferrite's magnetic characteristics are caused by interactions between metallic ions at particular sites in relation to oxygen ions in the oxide crystal structure. Between 1945 and 1993, Snoek and his colleagues at the Philips Research Laboratories in the Netherlands created a variety of ferrites. Based on their crystal structure and the molar ratio of Fe_2O_3 to other oxide components, ferrites are divided into four groups. The four types of ferrites are garnet ferrites, spinel ferrites, ortho ferrites, and hexagonal ferrites. Among other qualities, these ferrites stand out for their chemical stability, mechanical hardness, and electromagnetic strength. $CuFe_2O_4$ nanoparticles are the preferred spinel ferrite because of their capacity to change their physical characteristics under different environmental conditions, including phase transitions, electrical switching, semi-conductivity, magnetic properties, and chemical stability. $CuFe_2O_4$ nanoparticles come in two varieties: inverse and mixed spinel ferrite. $CuFe_2O_4$ nanoparticles have been used as anode materials for lithium-ion rechargeable batteries, energy storage materials, carbon dioxide reduction catalysts, coupling reaction catalysts, photoanodes for solar water oxidation, support for enzyme immobilization, photocatalysts for hydrogen evolution using visible light, and catalysts in nanomedicine for the treatment of breast cancer. Spinel ferrite nanoparticles can be

produced using co-precipitation, microemulsion sol-gel, citrate sol-gel, hydrothermal, the redox process, combustion, and other methods. Each of these synthesis techniques has advantages and disadvantages. Maensiri et al. described the white egg approach as a simple, affordable, and environmentally friendly way to produce transition metal-substituted ferrites in the form of spinel ferrite nanoparticles. Since egg white is a precursor, the reaction's hazardous effluents and toxic antecedents may be reduced (In 2023, P. Aji Udhaya et al.) [112].

2.4 Copper Oxide Doped Copper Ferrite Nanoparticles

Although it breaks down quickly because of the recombination of photoinduced charge carriers, copper ferrite absorbs the visible portion of the spectrum. Creating heterojunctions that with other semiconductor is a workable solution to this issue. The CuO/CuFe2O4 system is a common example. The p-type semiconductor CuO has a very small bandgap of 1.2 eV. Nevertheless, CuFe2O4, a typical n-type semiconductor, can form a p-n-heterojunction with improved photocatalytic capabilities by hybridizing with CuO. The two phases must make close, ideally ideal, contact across the interface for the heterojunction to grow. One-step or multi-step processes are used to create heterojunctions.

In the latter case, the components of the heterojunction are first obtained independently and then put together using a number of methods, such as casting, high-temperature solid-phase synthesis, impregnation, hydrothermal/solvothermal treatment, mechanochemical synthesis, sol–gel technology, hydrothermal/solvothermal treatment, and ultrasonic assembly. The disadvantages of this approach include the difficulty in obtaining a high-quality heterojunction boundary and the poor coupling between the components. Precursors of one or more components with the proper heterostructure are mixed and treated in the one-step process. Typically, a series of ionic reactions occur, with the resulting phases evenly distributed inside the heterostructured material Glazkova, E.A. et al. (2022) [113].

2.5 CO_2 Reduction

Climate change, which is brought on by the rapid increase in atmospheric CO_2, is one of the most pressing issues of our day. It's critical to lessen the accumulation of CO_2 in the atmosphere. Reducing the amount of CO_2 produced, utilizing CO_2, and storing CO_2 are the three methods for reducing CO_2 emissions. One preferred option

that meets the CO_2 recycling criteria is to convert CO_2 into chemicals. Photoreduction is one possible way to transform CO_2. Honda et al. first reported the photoreduction of CO_2 to organic molecules, such as HCOOH, HCHO, CH_3OH, and CH_4, in an aqueous solution of semiconductor powders in 1979. Many studies focused on the reduction of CO_2 using photocatalysis with H_2O. Due to the low solubility of CO_2 in water and the weak reducibility of water, a large number of extra reductants were used for the photoreduction of CO_2 (Qin Shiyue and others, 2011) [114].

2.6 Band Gap Energy

In order to absorb visible light, semiconductors must have a band gap energy that falls within a certain range. This energy is crucial for regulating the photocatalytic activity of nanomaterials. Due to their large band gap, the majority of metal oxide semiconductors cannot absorb visible light. However, because of rapid recombination, photogenerated holes and electrons cannot be used effectively for photocatalytic conversion in semiconductors with a narrow band gap. Doping heteroatoms, functionalizing photocatalysts, adding a co-catalyst to trap the photogenerated electrons or holes, and keeping an eye on the defect density in the semiconductor lattice can all postpone the recombination time.. Organic reducing agents such alcohols, triethanolamine, and triethylamine have been used as hole scavengers to oxidize holes. CO_2 can simultaneously be changed into the compounds by easily accessible photo-electrons. Using water and other protic solvents, CO_2 has also been photocatalytically hydrogenated. The active sites for CO_2 adsorption provided by catalysts based on nanostructural semiconductors allow photogenerated electrons to transform CO_2 into the proper products. Photocatalytic activity is facilitated and the conversion rate is increased by co-catalysts and photosensitizers (Gusain Rashid et al., 2016) [115].

Notwithstanding Cu's inherent poor activity for CH_3OH synthesis, Cu-based catalysts have attracted a lot of interest in the effort to convert CO_2 into CH_3OH. At moderate temperatures and pressures, the traditional Cu–ZnO catalyst, which consists of CuO, ZnO, and Al_2O_3 or ZrO_2, exhibits conversion efficiencies of about 30% and CH_3OH selectivity between 30% and 70%. Co-precipitation of metal hydroxycarbonates is the most common synthesis technique, and the hydroxycarbonate phases that are produced depend on variables including pH and temperature. Alternative techniques seek to improve catalyst stability and activity,

such as accessing amorphous georgeite via supercritical CO_2. Tuning active site activities and densities and improving traditional catalysts such as Cu–ZnO/ZrO_2 by spreading them over mesoporous supports or integrating them into layered hydrotalcite are examples of catalyst design methodologies [116].

In order to convert CO_2 to volatile fatty acids (VFAs), copper ferrite/reduced graphene oxide (CF/rGO) nanocomposites (NCs) were created using the bio-combustion process and used as cathode catalysts in microbial electrosynthesis systems (MES).

In comparison to CF alone, the NCs' raised surface area of CF/rGO (158.22 m^2/g) was 2.24 times greater, indicating a porous network-like structure. For CF/rGO/Carbon cloth (Cc), cyclic voltammetry (CV) and electrochemical impedance spectroscopy (EIS) tests showed a low charge transfer resistance of 2.8 Ω and a significant decrease in current density of −7.3 A/m^2. Field emission scanning electron microscopy (FESEM) revealed more rod-shaped bacteria on the cathode, demonstrating the CF/rGO catalysts' outstanding biocompatibility and multi-length scale porosity, which promotes microbial colonization. The predominant microbial communities on the cathode were Firmicutes, Bacteroidetes, and Proteobacteria (Betaproteobacteria), which were important in the bioelectrochemical reduction of CO_2 to VFAs. In order to facilitate effective MES performance and further the microbial reduction of CO_2 to valuable VFAs, our study highlights the potential of CF/rGO/Cc electrodes as conductive materials with exceptional electrochemical properties [117].

Using the eco-friendly oxidant H_2O_2, the sonocatalytic effectiveness of a recently created magnetic $CuFe_2O_4$/MIL-101/Graphene (CMG) ternary nanocomposite was investigated for the removal of organic dyes (methylene blue, rhodamine B, and methyl orange) from water. The CMG nanocomposite was created using a two-step hydrothermal method at 200 °C. Scanning electron microscopy, energy-dispersive X-ray spectroscopy, Fourier-transform infrared spectroscopy, magnetic measurements, atomic force microscopy, Brunauer–Emmett–Teller analysis, and Raman microscopy were used to evaluate the physical and chemical properties of the generated nanocomposite. The mechanisms of sonoluminescence and hot spots were credited with the CMG nanocomposite's exceptional sonocatalytic activity. A number of operational parameters were methodically investigated, such as the

catalyst dosage, pH, and starting dye concentration. The sonodegradation of dyes in the CMG suspension was found to be significantly influenced by hydroxyl radicals (•OH), according to trapping tests. The CMG nanocomposite could be easily detached with a magnet and repurposed without structural changes by utilizing the magnetic characteristics of $CuFe_2O_4$ nanoparticles [118]. Copper ferrite ($CuFe_2O_4$) nanoparticles (NPs) have recently caught the interest of researchers because of their possible uses in water purification. These NPs are stable in a range of circumstances and are distinguished by their low cost as a magnetic material. This characteristic makes it simple to recover treated water using an external magnetic field, allowing for repeated cycles of use. This focuses on comprehending how the magnetic properties of $CuFe_2O_4$ NPs and their nanocomposites (NCs) are influenced by several parameters, including the synthesis technique, calcination temperature, dopant type, pH, and crystalline size. $CuFe_2O_4$ NPs' potential for photocatalysis and adsorption in combination with other nanomaterials is highlighted by the exploration of their use in water treatment. There is discussion about the viability of recovering and recycling $CuFe_2O_4$ NPs and their NCs.

The review concludes by outlining the current research gaps in adjusting $CuFe_2O_4$ NPs' magnetic characteristics and other physical features for best use in water purification. The potential industrial application of $CuFe_2O_4$ NPs and their NCs for water purification is highlighted; they provide economical water treatment by using visible light as an energy source and being reusable [108].

CHAPTER 3

METHODOLOGY

3.1 Material

Sigma Aldrich supplied the chemicals sodium hydroxide (NaOH), copper nitrate ($Cu(NO_3)_2.2H_2O$), and iron (III) nitrate ($Fe(NO_3)_3.9H_2O$). No additional purification was done before using any of the chemicals. The top-notch university lab produced ethanol and deionized water.

3.2 Synthesis Of $CuFe_2O_4$ Nanoparticles

Pure copper ferrite was created via a sol-gel co-precipitation process [119]. In 100 milliliters of DI water, 0.2 M copper nitrate and 0.4 M iron nitrate were dissolved independently. With constant stirring, the copper nitrate solution was gradually added to the iron nitrate solution. 15.2 mmol CTAB was added after the nitrate salts had been dissolved in the DI water. After reaching the basic pH, 1M NaOH was added drop by drop to keep the pH between 10 and 11, while keeping the temperature at 60 °C and stirring the mixture for two hours without heating it. The solution was centrifuged to remove the $CuFe_2O_4$ product from water and excess salts while keeping the pH at a neutral level. The product was dried for 24 hours at 80°C in an oven, and the solid material was calcined for three hours at 500°C in an electric furnace. This sample was given CF NPs.

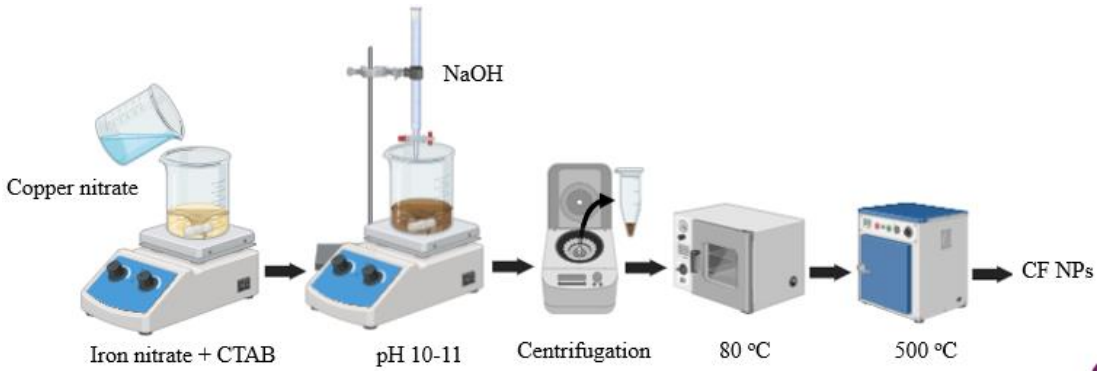

Figure 3.1 Synthesis of copper ferrite (CF NPs) nanoparticles

3.3 Synthesis Of CuO Nanoparticles

With few adjustments, copper oxide nanoparticles were created using a sol-gel combustion process [49]. After dissolving 4.57 g of $Cu(NO_3)_2 \cdot 3H_2O$ in 200 ml of DI water, 2 g of CTAB was added to the nitrate solution. After stirring the mixture for 30 minutes, 10 milliliters of sodium hydroxide was gradually added until the pH reached 10. After aging the solution for two to four hours while stirring, repeatedly wash it with ethanol and DI water to keep its pH balanced. An oven was used to dry the product for 24 hours at 70 degrees Celsius, and an electric furnace was used to calcine the solid material for two hours at 400 degrees Celsius. CuO nanoparticles weighing 1.51 g were produced.

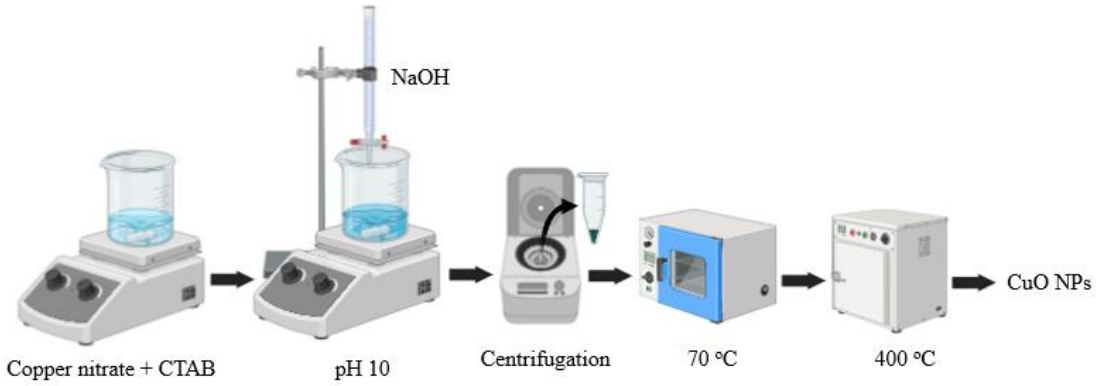

Figure 3.2 Synthesis of copper oxide (CuO) nanoparticles

3.4 Synthesis Of Copper Oxide Doped Copper Ferrite Nanocomposites

With few adjustments, a binary CuO-$CuFe_2O_4$ nanocomposites were created using the ultra-sonication process [120]. To create a final dispersion, 0.1 M $CuFe_2O_4$ and 0.1 M copper oxide nanoparticles were mixed in 200 ml of deionized water and ultrasonically agitated for an hour (Table 3.1). Centrifugation was used to gather the precipitates, which were then cleaned with ethanol and deionized water and dried in a vacuum desiccator for 24 hours at 80 ^oC. Binary nanocomposites of CuO-CF are the end result.

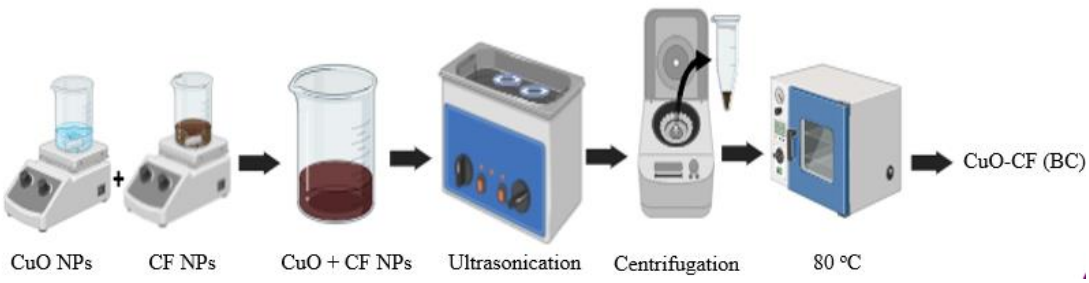

Figure 3.3 Synthesis of copper oxide doped copper ferrite binary composite (CuO-CF (BC))

Table 3.1 Ratio of binary composite formation

Binary composite	**Molarity**	**% age**	**Mass**
CuO-$CuFe_2O_4$	0.1 M	10 % CuO-90 % $CuFe_2O_4$	0.159g CuO-3.406g $CuFe_2O_4$

3.5 Characterization Techniques

Analysis was done using X-ray diffraction (XRD), scanning electron microscopy (SEM), and Fourier transform infrared (FT-IR) to ascertain the elemental makeup. The surface morphology of the nanocomposites was investigated using SEM, and the optical properties of the samples were assessed using a UV-vis (UV-visible) spectrometer. The size and shape of the nanocomposite, the degree of orientation of the nanoparticles in the matrix, and the crystalline phases are all determined using the XRD technique. Additionally, it was employed to examine the interfacial interactions between the nanoparticles and the matrix as well as the existence of defects. The FT-IR approach was used to examine the chemical surface and reactive sites of the nanoparticles.

3.6 Photocatalytic Activity Measurement

In order to investigate the photocatalytic reduction of CO_2 in the presence of photocomposites comprising different concentrations of CuO dopant over copper ferrite (CF) nanoparticles, CuO-CF composites were made using an optical reactor system. The experiment was carried out under a UV-Vis light source for six hours, as shown in Figure 3.4. The visible and ultraviolet light sources' intensities were measured using a Lux meter. Within the reactor, a quartz tube was placed in the center of a 12W UV lamp, producing a radiation source with an intensity of 3.5729 W/m^2. A 100W tungsten lamp was used as the visible light source and placed 5 cm in front of the reactor to introduce combined UV-Vis radiation [121]. One valve allowed gas to bubble, another allowed gas to evacuate and was attached to a pump that circulated CO_2 gas into the reactor, and a third valve allowed CO_2 to circulate

continuously. The fourth valve provided a sampling port for product analysis. The reaction temperature was maintained throughout, and the glass reactor was supported on a magnetic stirrer to guarantee a consistent suspension. Photocatalytic activity was determined at a pH of neutral, with the illumination temperature kept between 65 and 70 °C. The gas pressure was kept at roughly 30 psi during the reaction. A thermocouple was placed within the reactor and its tip made contact with the catalyst sample in order to detect temperature changes in real time. In order to confirm the photocatalytic process of CO_2 reduction, blank experiments were carried out in complete darkness, without any catalyst, and without UV-Vis light. Control experiments verified that the observed photocatalytic activity was caused by the presence of the CuO-CF catalyst in light-only conditions.

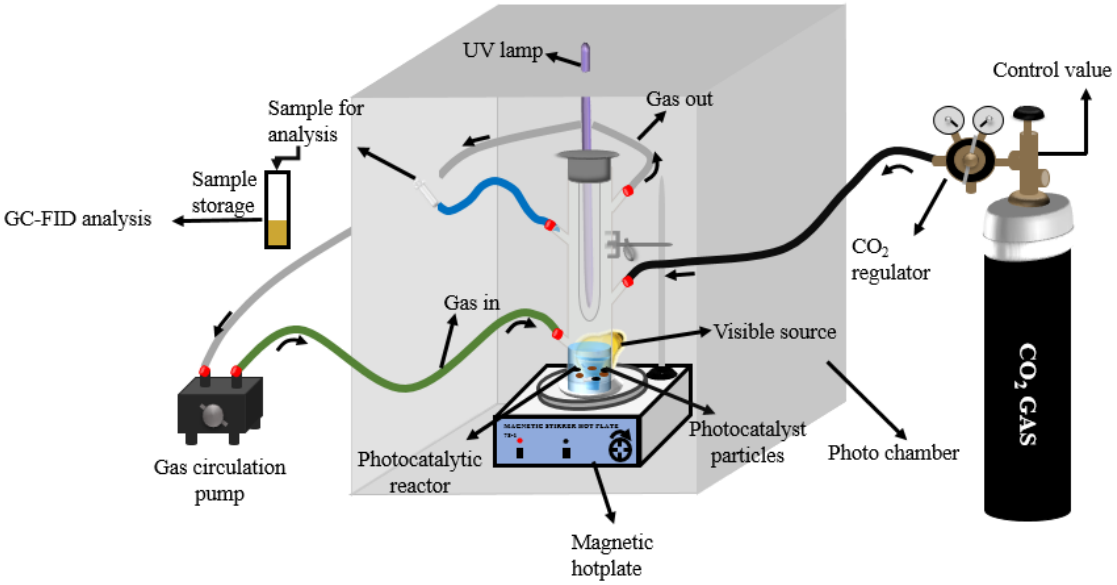

Figure 3.4 shows the experimental setup for the photocatalytic conversion of CO_2 to CH_3OH using a UV-Vis lamp as a radiation source

3.7 The Process Of Photocatalytic Reduction Of CO_2

The photocatalytic CO_2 reduction reactions were conducted in a specially designed glass reactor. A 0.2 g sample of synthesized CuO-doped copper ferrite (CuO-CF) photocatalyst was distributed using 80 mL of deionized (DI) water as the reducing media. The solution was constantly spun to guarantee a homogeneous suspension, and the pH was monitored and maintained at a neutral level throughout the experiment. Pure CO_2 gas was bubbled into the reactor solution for at least ten minutes before irradiation in order to replace any dissolved oxygen and fully saturate

it with CO_2. After saturation was verified, the photoreduction process was initiated by turning on both visible and UV light at the same time.

For the duration of the photocatalytic reaction, CO_2 was continuously bubbled in the reactor at a constant flow rate of 0.15 mL/min and a maintained gas pressure of about 30 psi. To collect scattered catalyst particles, liquid-phase samples were collected hourly using a 5 mL syringe equipped with a membrane filter. Through sample analysis, the concentration of photocatalytic reduction products was ascertained. Liquid items were quantitatively analyzed using gas chromatography (Agilent 6890N with Head-space Sampler G1888, USA) with polyethylene glycol and a DB-Wax column as the stationary phase and a Flame Ionization Detector (GC-FID). The carrier gas was high-purity nitrogen gas (99.995%) [122]. The liquid product that was mainly investigated was methanol (CH_3OH).

A calibration curve was made using a known standard quantity of methanol in order to determine the unknown amounts of photocatalytic samples. The MDL for methanol detection was established at 25 ppm, the lowest concentration that generated detectable signals under the existing GC-FID conditions [123].

CHAPTER 4

RESULTS

4.1 Optical Analysis

4.1.1 Ultraviolet-Visible Spectroscopy (UV-Vis)

The UV-visible spectroscopy approach was used to examine the optical properties of as-prepared nanoparticles, such as CF, CuO, and CuO–CF binary composite. These nanoparticles were ultrasonically dissolved in pure ethanol prior to measurement. The UV-Vis spectrophotometer was used to measure their absorption spectra. A higher surface-to-volume ratio results in a greater surface density of flaws, which raises the optical absorption. The copper ferrite (CF) nanoparticles showed high absorption at around 348 nm, indicating involvement in charge transfer transitions, as a result of the d–d electronic transitions of the Cu^{2+} and Fe^{3+} ions (Figure 4.1 (a)). However, CF nanocrystals exhibited minimal photocatalytic activity in the visible range because of their UV-dominated absorption nature [124]. CuO nanoparticles' UV-Vis absorption spectra showed a single, noticeable absorption peak at roughly 275 nm, which is a typical band of CuO (Figure 4.1 (b)). This significant blue shift relative to bulk CuO is caused by the quantum confinement effect induced by the nanometer scale. Due to internal crystal field effects or lattice distortion, CuO absorbance coefficient decreased as wavelength increased, a feature common to many semiconductor materials [125]. On the other hand, with a peak range of roughly 410 nm, the CuO-doped CF (CuO–CF) binary composite demonstrated enhanced light absorption in the visible and UV regions (Figure 4.1 (c)). The enhanced absorption spectrum in CuO–CF is due to the synergistic effect of CuO and CF nanoparticles, which enhances sustained light-harvesting capabilities. The enhancement provides better photocatalytic ability for CO_2 reduction under UV-Vis irradiation [126]. Ahmed et al. determined that the optimal UV-Vis spectrum range for photocatalytic CO_2 reduction was between 300 and 430 nm [127].

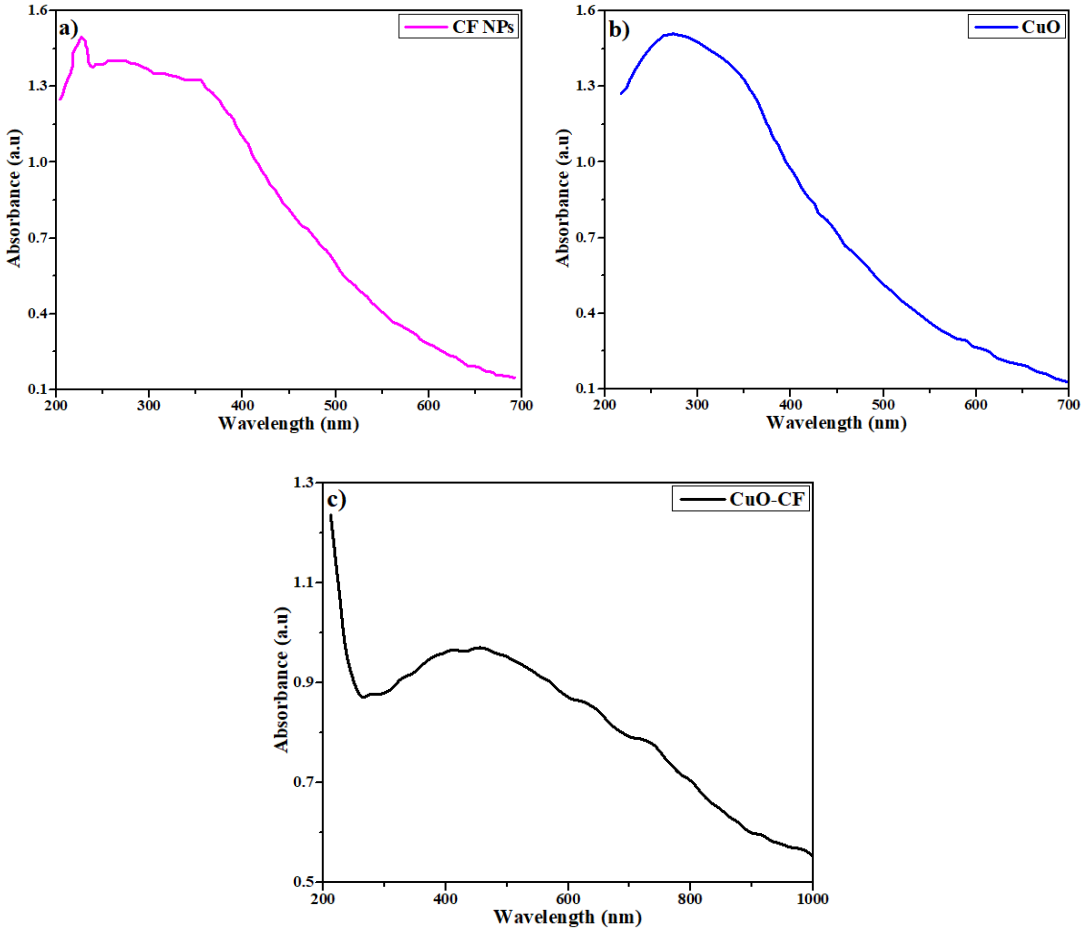

Figure 4.1 UV-Vis spectrum analysis of: (a) CF, (b) CuO, and (c) CuO-CF (BC)

Bad-Gap:

Using the Tauc plot based on UV-Vis absorbance data, the band gap energy (Eg) of each sample was calculated using the following formula:

$$(\mathbf{hv})^2 = \mathbf{A}\ (\mathbf{hv} - \mathbf{E_g}) \quad (1)$$

Where: α

α = absorption coefficient, which is determined using

$$\boldsymbol{\alpha} = \boldsymbol{\pi k}/\lambda \quad (2)$$

n is equal to ½ for indirect transitions and 2 for direct transitions, where hv is the photon energy and A is the proportionality constant.

The linear component of the Tauc plot was extrapolated to the x-axis (hv) to yield the following Eg values for the materials: CF nanoparticles showed appropriate band alignment for photocatalytic applications with a band gap of 1.39 eV (Figure 4.2 (a)), which was very close to values documented in the literature. It is marginally lower than previously published values (e.g., 1.42 eV of Kezzim A et al.) because of perhaps bigger crystallites. Figure 4.2 (b) shows that the band gaps of CuO nanoparticles were 2.18 eV, which is well within the reported range of 1.8 to 2.5 eV for CuO. The tiny variations are caused by synthesis techniques and influences of nanoparticle size; the band gap is somewhat blue-shifted because the quantum confinement effect is greater for smaller particles [125]. Marotti et al. claim that larger crystallite sizes lead to a lower band gap. The 1.64 eV band gap of the CuO–CF binary composite supports its ability to absorb visible and UV light (Figure 4.2 (c)). The modest band gap, which offers the ideal energy barrier for electron transport and excitation, boosts the efficiency of the photocatalytic CO_2 reduction process. The CuO and CF interaction improves interfacial charge separation, reduces electron-hole recombination, and promotes charge mobility, making the binary system superior to its component parts [124].

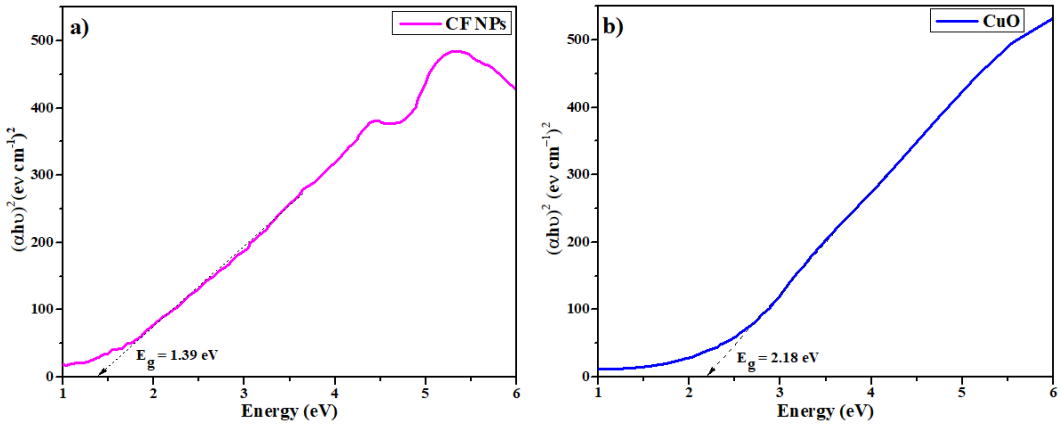

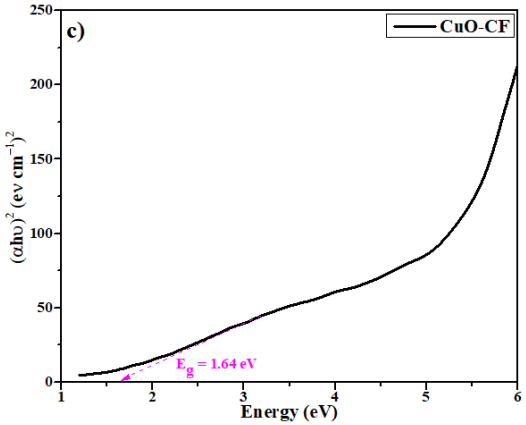

Figure 4.2 Tauc‟s plot to estimate band gap energies (E_g) of synthesized nanoparticles: (a) CF NPs, (b) CuO, and (c) CuO-CF (BC)

4.1.2 Photoluminescence Spectroscopy (PL)

Electron-hole (ē/h+) pair recombination, migration, and trapping effectiveness in photocatalytic materials were all examined using PL emission spectra. Decreased PL intensity emissions are associated with a decreased ē/h+ pair recombination rate. All of the necessary samples' intensities were qualitatively assessed under the same experimental setup. Last but not least, a PL experiment was conducted for CF NPs in conjunction with CuO and CuO-CF in the range of 300-800 nm wavelength light source in order to comprehend the charge separation behavior in hybrid catalysts surface. The data obtained from this experiment is displayed in Figure 4.3. The likelihood of strong photogenerated charge recombination on the CF NPs photocathode surface is indicated by a sharp emission peak detected in the CF NPs at 486 nm [128]. At an excitation wavelength of 460 nm, a prominent emission peak for the CuO and the CuO–CF binary composite was observed at 482 nm. Oxygen vacancies, surface effects, interstitial ion effect, and electron recombination between the donor and acceptor level defects of the nanoparticles may be the cause of the peaks displayed by the p-type semiconductor copper oxide nanoparticles [129].

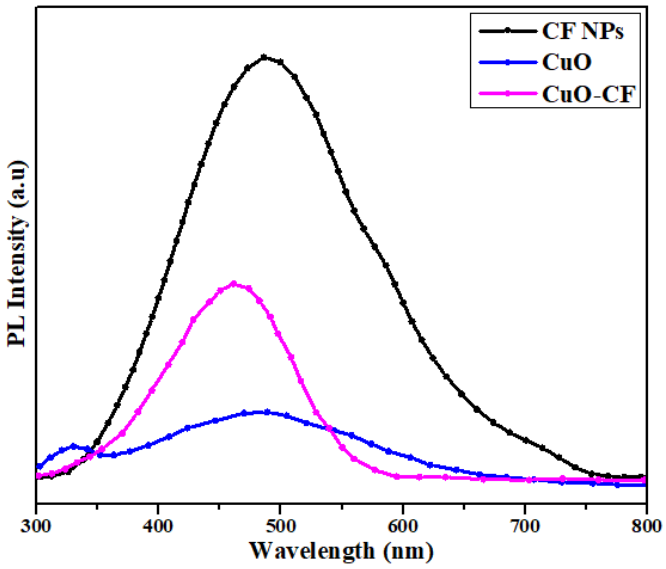

Figure 4.3 PL emission spectra /spectral analysis of CF NPs, CuO, and CuO-CF (binary composite)

4.2 Structural Techniques

4.2.1 FT-IR

Figure 4.4 (a, b) shows the FTIR spectra of the $CuFe_2O_4$, CuO, and CuO-$CuFe_2O_4$ nanoparticles, which were recorded in the 4000–400 cm^{-1} range. The FTIR spectra of $CuFe_2O_4$ nanoparticles are displayed in Figure 4.4 (a). At 2972.33 cm^{-1} and 2900.27 cm^{-1}, the band vibrations O–H interacting through H-bonds were detected. In the low wavelength region, the peaks displayed the distinctive peaks of spinel-made ferrites, with the MO (M) vibrations represented by Cu or iron at 694.56 cm^{-1}, 598.93 cm^{-1}, 534.97 cm^{-1}, and 430.2 cm^{-1} [130]. Infrared spectroscopy of copper oxide nanoparticles is displayed in Figure 4.4 (a). This figure shows that there are five peaks. The O-H stretching, O-H bending of a hydroxyl group, C–O asymmetric, C–O symmetric, and Cu–O bond are the factors associated with the peaks at 3590.97, 1620.51, 1380.21, 1134.23, and 511.97 cm^{-1} wave number, respectively [131]. The FT-IR spectra of the CuO-CF binary composite are displayed in Figure 4.4 (b). The stretching vibration bands of the O-H functional group are responsible for the distinctive absorption band of 3340.73 cm^{-1}. The presence of O-H bending and C-H bond properties allows for the observation of the bands at 1543.33 and 694.56 cm^{-1}.

510.3 cm^{-1} is where the significant absorption peaks the presence of Cu-O and Fe-O vibrations allows for the observation of 470.56 cm^{-1} [132].

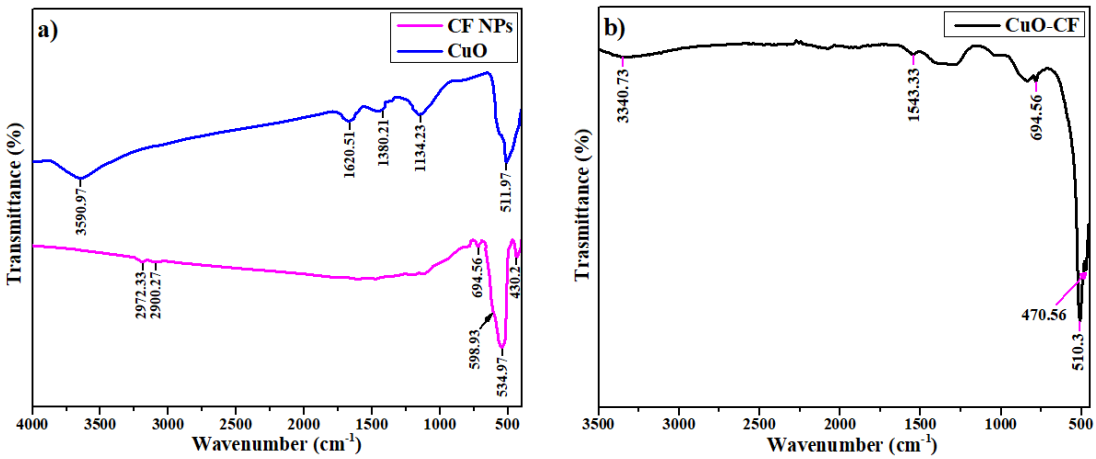

Figure 4.4 FT-IR spectra of CF NPs, CuO nanoparticles (a), CuO-CF binary composite (b)

4.2.2 XRD

The XRD pattern of the CF NPs, CuO, and CuO-$CuFe_2O_4$ binary composite is displayed in Figure 4.5. [133]. The CF NPs X-ray diffraction pattern included a number of intense diffraction 2θ angles at 29.92, 36.68, 48.5, 57.2, 60.4, 65.12, 73.4, and 88.04°. XRD analysis was used to identify the CuO pearls' crystallinity and crystal phases. With miller indices of (111) hkl value, the main peak of CuO is indexed at 2θ = 52.3°. A few more CuO peaks may be seen at 32.69° (110), 36.68° (002), 58.06° (112), 64.71° (202), 73.8° (113), 77.23° (311), 85.02° (222), and 87.66° (310). Only the pure monoclinic phase of CuO is visible in the produced nanoparticles upon notification reflection peaks, and this value is in good agreement with the value found in the literature (JCPDS card No. 05-0661) [134, 135]. XRD pattern for the ultrasonic power-synthesized magnetic composite (CuO-CF) sample. It is seen that the entire peaks in this pattern match the usual pattern of copper oxide and copper ferrite, confirming their presence in the binary composite as synthesized [133].

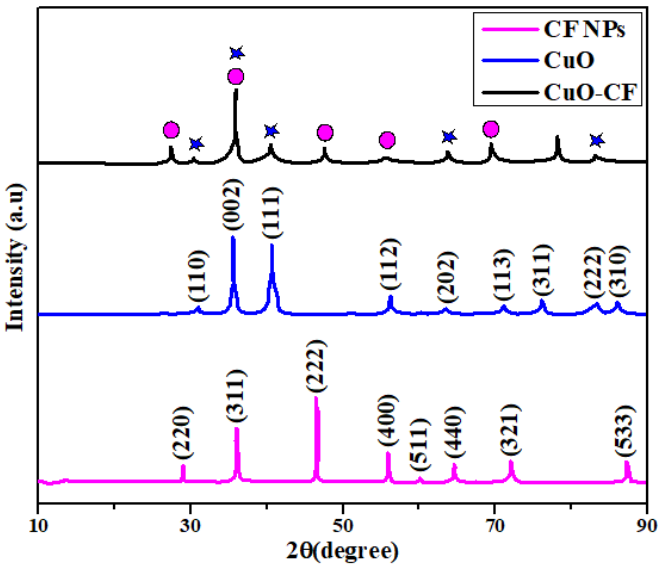

Figure 4.5 X-ray diffraction patterns of CF NPs, CuO and CuO-CF

4.2.3 Energy-Dispersive X-Ray Spectroscopy (EDX)

The Bruker model EDX instrument was also used to determine the elemental compositions of the copper ferrite, copper oxide, and copper oxide doped copper ferrite binary composites and nanoparticle components. The elements copper, iron, and oxygen are confirmed to be present in $CuFe_2O_4$ by the EDX analysis (see Figure 4.6 (a)). In addition, it was determined that the atomic ratio of Cu:Fe was 25.89%:53.49% with an uncertainty of ±1.90%. For the chemical formula $CuFe_2O_4$, the expected atomic ratio of 1:2 is nearly met by the Cu:Fe atomic ratio as found by EDX analysis. It was also found that the atomic percentage of oxygen in $CuFe_2O_4$ was 20.63%. The presence of the copper and oxygen components in the CuO is further confirmed by the EDX spectrum shown in Figure 4.6 (b). Additionally, it was found that the atomic ratio of Cu:O was 48.02%:51.98% with a ±2.98% uncertainty. For the molecular formula CuO, this ratio is extremely near to the theoretically predicted value of 1:1 [49]. The successful production of the binary composite (CuO-CF) was confirmed by the presence of Cu and Fe, which defined the formation of copper and ferrite oxide [117].

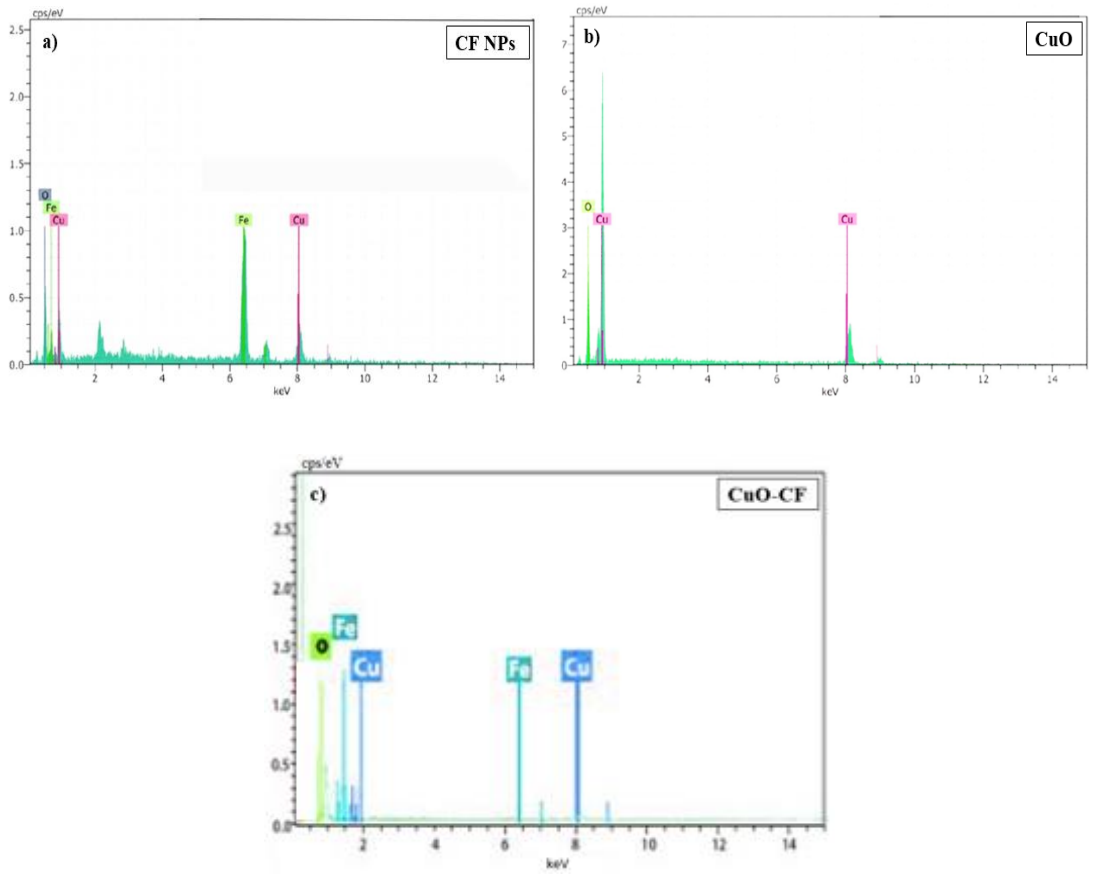

Figure 4.6 The EDX spectrum of the CF NPs (a), CuO (b), and CuO-CF (c)

4.3 Morphological Techniques

4.3.1 SEM

The Zeiss Supra 40VP type Scanning Electron Microscope (SEM) measurements were used to analyze the samples' surface morphology. The SEM pictures of the powder-formed samples are shown in Figure 4.7. The nearly spherical particles that make up CF NPs are equally dispersed throughout the crystalline structure and have a size in the nanometer range, as shown in Figure 4.7 (a). The copper ferrite nanoparticles' spherical form is consistent with the scientific literature [136]. An image of nearly uniformly dispersed CuO nanoparticles with urchin-like morphology can be found in Figure 4.7 (b) [137]. Because the copper oxide nanoparticles in CF nanoparticles are distributed randomly, the binary composites have a rougher surface, as seen in Figure 4.7 (c). Additionally, the urchin-like structure of CuO

nanoparticles is visible in the micrographs when the weight fraction of CuO nanoparticles in the composites increases.

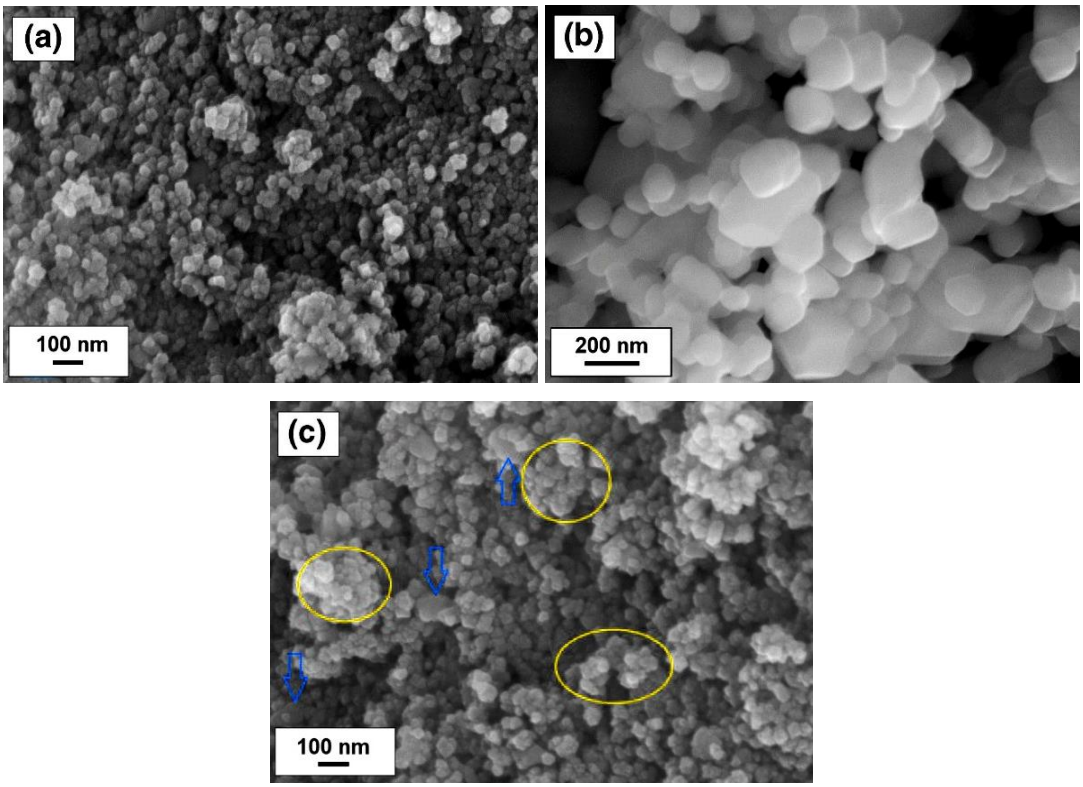

Figure 4.7 SEM micrographs of CF NPs (a), CuO (b), and CuO-CF binary composite (c).

4.4 Photocatalytic Activity

We conducted a number of control tests to make sure that the synthesis of methanol would result from the photocatalytic reduction of carbon dioxide. These tests included 1) one in which carbon dioxide was not introduced into the photocatalytic reactor; 2) one without any visible or ultraviolet light source; 3) one without the photocatalyst that was added to the reactor; and 4) one without the use of water as a reducing agent. There are no products to identify since the impurities, not the CO_2, must be the source of the products in such an experiment [138]. To avoid overestimating product production, the amount of product identified in the real CO_2 reduction is adjusted by the amount in the blank operation if product formation is

detected [139]. When all the requirements were met, methanol was formed (Table 4.1).

Table 4.1 Elucidates sundry control experiment to affirm the source of carbon-based compounds, X = Without particular substance, ☑ = Sign shows availability of particular reactants

Experiment No	Reaction Conditions				Methanol Formulation
	CO_2	Light Intensity	Photocatalyst	Reducing Agent	
1	X	☑	☑	☑	X
2	☑	X	☑	☑	X
3	☑	☑	X	☑	X
4	☑	☑	☑	X	X
5	☑	☑	☑	☑	☑

To do this, 0.5g of photocatalyst—which acts as a reducing agent by supplying electrons to aid reduction—was dissolved in 80mL of water. The photocatalytic photoreactor was purged at pressures beginning at 30 Psi while maintaining a steady flow rate of 0.15 mL/min. The catalyst surface was kept 5 cm from the illumination, and the light was evenly distributed throughout the reactor walls at an intensity of about 3.5729 W/cm^2 [121]. For every composition of the photocatalytic nanocomposite, liquid samples were taken over the course of an hour, and the reaction lasted for about five hours. Hourly liquid samples were analyzed using a GC-FID (Agilent 6890N with Head-space Sampler G1888, USA) with a polyethylene glycol stationary phase and a DB-Wax Column. Nitrogen, which was 99.995% pure, served as the carrier gas for the analysis [140]. The possibility for detecting gaseous molecules like CO, CH_4, H_2, etc. was not investigated in our studies; instead, we solely looked at the generation of liquid products. To ascertain the unknown content of the finished product and the linear response of the detector to a specific component, the calibration curve for methanol at various concentrations was plotted. The Minimum Detection Limit (MDL) for methanol was determined to be 25 mg/mL, the lowest response value found [141].

4.5 Photocatalytic CO_2 Reduction Performance

The methanol yield for CF NPs, CuO, and CuO-CF binary composite was plotted against time in order to determine the photocatalytic activity for the synthesis of solar fuels. In comparison to CF NPs and CuO, which were found to have yields of around 0.025 and 0.040 mmol g^{-1} h^{-1}, respectively, CuO-CF had the highest yield (0.12 mmol $g^{-1}h^{-1}$). The table displayed the photocatalysts' methanol yield. Rapid charge carrier recombination and restricted electron transport result in the lowest yield of CF NPs. Because of the large amount of oxygen atoms in their electronic structure, CF NPs have a defect that prevents electrons from traveling freely, which lowers their quantum efficiency (Table 4.2) [142].

The following formula was used to determine the rate of methanol yield [143].

$$Yield = \frac{Con.of\ product\ (parts\ per\ million)\ \times\ Volume\ of\ Solution\ (liter)}{Mass\ of\ photocatalyst\ (gram)\ \times\ Reaction\ time\ (Hours)}$$

The provided expression can be used to evaluate the quantum efficiency or yield [122].

$$QE = \frac{No.of\ \ moles\ (product)\ \times\ No.of\ e^{-1}\ (required)}{No.of\ Photons\ (absorbed)}\ x\ 100$$

$$QE = \frac{No.of\ \ moles\ (\frac{mol}{L})\ *\ 6\ *\ NA}{IE\ \times\ A\ \times\ \lambda\ \times \mathrm{T}\ \times h\ \times C}$$

where A stands for photocatalyst irradiated area (0.00321 m^2), IE for light intensity (3.5729 W/cm^2), λ for the light wavelength that was bombarded (>400 nm for visible light), h for plank's constant (6.634 × 10-34 J.s), C for light speed (3 × 108 $m.s^{-1}$), T for reaction time in seconds (3600 s), and NA for Avogadro's number (6.02 × 1023).

Table 4.2 Photoreduction of CO_2 into methanol under certain controlled experimental conditions

Sample	**Reaction Precursor**	**Reducing Agent**	**Visible/UV Light (nm)**	**Time (hour)**	**Methanol Yield (mmol/gh)**	**Quantum Efficiency$_{max}$ (%)**
CF NPs	CO_2	H_2O	400/267	4	0.025	0.5

CuO	CO_2	H_2O	400/267	4	0.040	1.2
CuO-CF	CO_2	H_2O	400/267	4	0.120	3.5

4.6 Effect Of Pressure On CO_2 Photoreduction

The CO2 pressure was raised from 30 kPa to 180 kPa in order to use photocatalysis to convert carbon dioxide into methanol. According to the graph, photoreduction of carbon dioxide increased to about 90 kPa. This could be because the higher concentration of carbon dioxide in the photocatalytic system made it easier for carbon dioxide to be converted into solar fuels like methanol and formic acid. As the pressure increases, more carbon dioxide enters the reaction system and diffuses more readily to the catalyst surface's reactive active sites. Additionally, the increased pressure prevents catalyst poisoning by halting backward reduction reactions on the catalyst surfaces. Figure 4.8 illustrates how the production rate (mmol/gh) and quantum efficiency (%) dropped above 90 kPa and up to 180 kPa. This could be explained by the fact that carbon dioxide was unable to adhere because unstable and ineffective byproduct molecules occupied reactive active sites. Therefore, absorption must occur at the ideal pressure (Poptimum) for carbon dioxide to be converted to methanol.

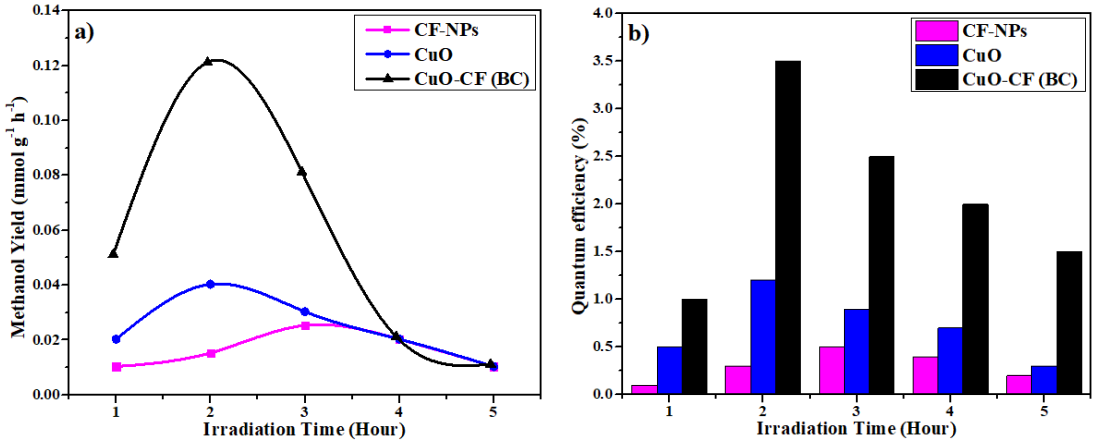

Figure 4.8 Photocatalytic CO_2 reduction (a) Methanol yield, and (b) quantum efficiency

CHAPTER 5

DISCUSSION

The photocatalytic evaluation and synthesis of copper ferrite (CF), copper oxide (CuO), and their binary composite (CuO–CF) nanoparticles have yielded results about their appropriateness for photocatalytic CO_2 reduction to methanol (CH_3OH) production. The binary composite's superior structural, optical, and electronic properties allowed it to perform noticeably better than the other produced compounds, as shown by UV-Vis spectroscopy, FT-IR, XRD, SEM, EDX, and PL studies. First, it was shown that pure copper ferrite nanoparticles (CF NPs) produced using the ultrasonication method had a limited ability to use photocatalysis to decrease CO_2. This reduced activity is caused by its relatively narrow visible region absorption, high electron-hole recombination rate as indicated by PL spectra, and less ideal form as seen by SEM images. Additionally, although the predicted band gap for CF was within the acceptable range for visible-light photocatalysis, it was at 1.38 eV, which did not lead to effective photoinduced charge separation or transfer. UV-Vis research revealed moderate absorption at 354 nm by d–d transitions in Cu^{2+} and Fe^{3+} ions; nevertheless, this was not enough to start an effective photocatalytic activity. To overcome these limitations, a CuO–CF binary composite was made by combining copper ferrite with copper oxide (CuO), a strong visible light absorber with an appropriate band gap (~2.18 eV). This strategy was predicated on the notion that CuO doping would enhance light harvesting capacity, quench charge carrier recombination, and increase surface defect features (such oxygen vacancies), all of which are critical for effective CO_2 photoreduction. The resultant CuO–CF binary composite showed better photocatalytic activity than either of their individual counterparts. The composite's UV-Vis absorption expanded widely into the visible spectrum with redshift at its maximum, suggesting better light utilization. The composite's band gap (~1.64 eV) was within the optimal region for CO_2 photoreduction, suggesting better charge mobility and a lower energy barrier for

photogenerated electron transfer. PL analysis revealed less recombination in the binary system, however SEM images revealed more distinct and connected nanostructures, providing more surface area for catalytic activities. EDX verified the uniform distribution of Cu and Fe elements in the binary matrix. Most importantly, improved. Pristine CF NPs lacked this synergy, which led to lower conversion rates. According to previous studies, the optimization obtained through the creation of binary composites supports the notion that heterojunction or composite photocatalysts significantly outperform single-phase materials. The findings of this study were consistent with earlier studies that emphasize the crucial role that surface oxygen vacancies and heterostructure interfaces play in boosting photocatalytic activity.

CONCLUSIONS

This study investigated the synthesis, characterization, and photocatalytic activity of copper ferrite (CF), copper oxide (CuO), and their binary composite CuO-doped copper ferrite (CuO–CF) nanoparticles for the aim of photoreducing CO_2 to methanol (CH_3OH). Nanostructured materials were successfully created using a mix of chemical and ultrasonication procedures, and they were evaluated using FT-IR, XRD, SEM, EDX, PL, GC-FID, and UV-Vis spectroscopy methods. Copper ferrite nanoparticles exhibited inadequate photocatalytic activity due to substantial electron-hole recombination and inefficient visible light absorption, as indicated by PL results and the poor CH_3OH output from GC-FID analysis. The CF catalyst had a low band gap of 1.38 eV and was insufficiently active to convert CO_2 effectively when exposed to light. In order to overcome these limitations, a CuO–CF binary hybrid was produced by adding copper oxide to the CF matrix. The adjustment led to an improved band gap of 1.64 eV and improved light harvesting capabilities. The structural integrity and homogeneity of the composite were verified by the use of characterization techniques. UV-Vis examination revealed a red shift in absorption, while PL data verified a decrease in recombination. CuO–CF's photocatalytic activity was noticeably higher than CF alone, as seen by the enhanced methanol output.

REFERENCES

1. Narayanan KB, Sakthivel N. Biological synthesis of metal nanoparticles by microbes. Adv Colloid Interface Sci. 2010;156(1-2):1-13.
2. Thakkar KN, Mhatre SS, Parikh RY. Biological synthesis of metallic nanoparticles. Nanomedicine: nanotechnology, biology and medicine. 2010;6(2):257-62.
3. Taylor E, Webster TJ. Reducing infections through nanotechnology and nanoparticles. International journal of nanomedicine. 2011:1463-73.
4. Govindaraju K, Basha SK, Kumar VG, Singaravelu G. Silver, gold and bimetallic nanoparticles production using single-cell protein (Spirulina platensis) Geitler. Journal of Materials Science. 2008;43(15):5115-22.
5. Lengke MF, Fleet ME, Southam G. Biosynthesis of silver nanoparticles by filamentous cyanobacteria from a silver (I) nitrate complex. Langmuir. 2007;23(5):2694-9.
6. Rautaray D, Ahmad A, Sastry M. Biosynthesis of CaCO3 crystals of complex morphology using a fungus and an actinomycete. Journal of the American Chemical Society. 2003;125(48):14656-7.
7. Scarano G, Morelli E. Characterization of cadmium-and lead-phytochelatin complexes formed in a marine microalga in response to metal exposure. Biometals. 2002;15:145-51.
8. Kowshik M, Deshmukh N, Vogel W, Urban J, Kulkarni SK, Paknikar K. Microbial synthesis of semiconductor CdS nanoparticles, their characterization, and their use in the fabrication of an ideal diode. Biotechnology and bioengineering. 2002;78(5):583-8.
9. Anshup, Venkataraman JS, Subramaniam C, Kumar RR, Priya S, Kumar TS, et al. Growth of gold nanoparticles in human cells. Langmuir. 2005;21(25):11562-7.
10. Buzea C, Pacheco II, Robbie K. Nanomaterials and nanoparticles: sources and toxicity. Biointerphases. 2007;2(4):MR17-MR71.
11. Pal SL, Jana U, Manna PK, Mohanta GP, Manavalan R. Nanoparticle: An overview of preparation and characterization. Journal of applied pharmaceutical science. 2011(Issue):228-34.
12. Modi K, Raval P, Pansara P, Badi I, Devmurari D, Munshi S, et al. On the Relationship Between Structural-Optical Parameters of Y 3− x Fe 5+ x O 12 Garnet Ferrites and the Oxide Additivity Rule. Journal of Superconductivity and Novel Magnetism. 2016;29:1931-6.
13. Akhtar MN, Sulong A, Ahmad M, Khan MA, Ali A, Islam M. Impacts of Gd–Ce on the structural, morphological and magnetic properties of garnet nanocrystalline ferrites synthesized via sol–gel route. Journal of Alloys and Compounds. 2016;660:486-95.

14. Nakajima T, Tokunaga Y, Taguchi Y, Tokura Y, Arima T-h. Piezomagnetoelectric effect of spin origin in dysprosium orthoferrite. Physical Review Letters. 2015;115(19):197205.
15. Reid A, Rasing T, Pisarev R, Dürr H, Hoffmann M. Terahertz-driven magnetism dynamics in the orthoferrite DyFeO3. Applied Physics Letters. 2015;106(8).
16. Valenzuela R. Novel applications of ferrites. Physics Research International. 2012;2012(1):591839.
17. Litsardakis G, Manolakis I, Serletis C, Efthimiadis K. Effects of Gd substitution on the structural and magnetic properties of strontium hexaferrites. Journal of magnetism and magnetic materials. 2007;316(2):170-3.
18. Pullar RC. Hexagonal ferrites: a review of the synthesis, properties and applications of hexaferrite ceramics. Progress in Materials Science. 2012;57(7):1191-334.
19. Reddy DHK, Yun Y-S. Spinel ferrite magnetic adsorbents: alternative future materials for water purification? Coordination Chemistry Reviews. 2016;315:90-111.
20. Taffa DH, Dillert R, Ulpe AC, Bauerfeind KC, Bredow T, Bahnemann DW, et al. Photoelectrochemical and theoretical investigations of spinel type ferrites (M x Fe3− x O4) for water splitting: a mini-review. Journal of Photonics for Energy. 2017;7(1):012009-.
21. Silva VD, Ferreira LS, Simões TA, Medeiros ES, Macedo DA. 1D hollow MFe2O4 (M= Cu, Co, Ni) fibers by Solution Blow Spinning for oxygen evolution reaction. Journal of colloid and Interface Science. 2019;540:59-65.
22. Kefeni KK, Mamba BB, Msagati TA. Application of spinel ferrite nanoparticles in water and wastewater treatment: a review. Separation and Purification Technology. 2017;188:399-422.
23. Guijarro N, Bornoz P, Prévot M, Yu X, Zhu X, Johnson M, et al. Evaluating spinel ferrites MFe 2 O 4 (M= Cu, Mg, Zn) as photoanodes for solar water oxidation: prospects and limitations. Sustainable Energy & Fuels. 2018;2(1):103-17.
24. Kaur R, Hasan A, Iqbal N, Alam S, Saini MK, Raza SK. Synthesis and surface engineering of magnetic nanoparticles for environmental cleanup and pesticide residue analysis: a review. Journal of separation science. 2014;37(14):1805-25.
25. Ngomsik A-F, Bee A, Draye M, Cote G, Cabuil V. Magnetic nano-and microparticles for metal removal and environmental applications: a review. Comptes Rendus Chimie. 2005;8(6-7):963-70.
26. Ramimoghadam D, Bagheri S, Abd Hamid SB. Stable monodisperse nanomagnetic colloidal suspensions: an overview. Colloids and Surfaces B: Biointerfaces. 2015;133:388-411.
27. Parsons J, Lopez M, Peralta-Videa J, Gardea-Torresdey J. Determination of arsenic (III) and arsenic (V) binding to microwave assisted hydrothermal synthetically prepared Fe3O4, Mn3O4, and MnFe2O4 nanoadsorbents. Microchemical Journal. 2009;91(1):100-6.
28. Jacob NM, Kuruva P, Madras G, Thomas T. Purifying water containing both anionic and cationic species using a (Zn, Cu) O, ZnO, and cobalt ferrite based

multiphase adsorbent system. Industrial & Engineering Chemistry Research. 2013;52(46):16384-95.
29. Song Q, Zhang ZJ. Correlation between spin− orbital coupling and the superparamagnetic properties in magnetite and cobalt ferrite spinel nanocrystals. The Journal of Physical Chemistry B. 2006;110(23):11205-9.
30. Ateia EE, El-Bassuony AA, Abdelatif G, Soliman FS. Novelty characterization and enhancement of magnetic properties of Co and Cu nanoferrites. Journal of Materials Science: Materials in Electronics. 2017;28:241-9.
31. Hill RJ, Craig JR, Gibbs G. Systematics of the spinel structure type. Physics and chemistry of minerals. 1979;4(4):317-39.
32. Hajalilou A, Mazlan SA. A review on preparation techniques for synthesis of nanocrystalline soft magnetic ferrites and investigation on the effects of microstructure features on magnetic properties. Applied Physics A. 2016;122:1-15.
33. Chinnasamy C, Narayanasamy A, Ponpandian N, Chattopadhyay K, Shinoda K, Jeyadevan B, et al. Mixed spinel structure in nanocrystalline NiFe 2 O 4. Physical Review B. 2001;63(18):184108.
34. Manikandan A, Durka M, Seevakan K, Antony SA. A novel one-pot combustion synthesis and opto-magnetic properties of magnetically separable spinel Mn x Mg 1− x Fe 2 O 4 (0.0≤ x≤ 0.5) nanophotocatalysts. Journal of Superconductivity and Novel Magnetism. 2015;28:1405-16.
35. Rashad M, Mohamed R, Ibrahim M, Ismail L, Abdel-Aal E. Magnetic and catalytic properties of cubic copper ferrite nanopowders synthesized from secondary resources. Advanced Powder Technology. 2012;23(3):315-23.
36. Gomes J, Sousa M, Da Silva G, Tourinho F, Mestnik-Filho J, Itri R, et al. Cation distribution in copper ferrite nanoparticles of ferrofluids: A synchrotron XRD and EXAFS investigation. Journal of Magnetism and Magnetic Materials. 2006;300(1):e213-e6.
37. Zaki H, Al-Heniti SH, Hashhash A. Effect of Al3+ ion addition on the magnetic properties of cobalt ferrite at moderate and low temperatures. Journal of Magnetism and Magnetic Materials. 2016;401:1027-32.
38. Issa B, Obaidat IM, Albiss BA, Haik Y. Magnetic nanoparticles: surface effects and properties related to biomedicine applications. International journal of molecular sciences. 2013;14(11):21266-305.
39. Hsu C, Chen H. Developed in-situ X-ray spectroscopy to investigate the catalyst system toward oxygen evolution reaction. SPring-8/SACLA. 2017;22(4):297-305.
40. Guajardo-Pacheco MJ, Morales-Sánchez J, González-Hernández J, Ruiz F. Synthesis of copper nanoparticles using soybeans as a chelant agent. Materials letters. 2010;64(12):1361-4.
41. Xi Y, Hu C, Gao P, Yang R, He X, Wang X, et al. Morphology and phase selective synthesis of CuxO (x= 1, 2) nanostructures and their catalytic degradation activity. Materials Science and Engineering: B. 2010;166(1):113-7.
42. He Y. A novel solid-stabilized emulsion approach to CuO nanostructured microspheres. Materials research bulletin. 2007;42(1):190-5.
43. Motoyoshi R, Oku T, Suzuki A, Kikuchi K, Kikuchi S, Jeyadevan B, et al. Fabrication and characterization of cuprous oxide: fullerene solar cells. Synthetic metals. 2010;160(11-12):1219-22.

44. Dabagh S, Chaudhary K, Haider Z, Ali J. Study of structural phase transformation and hysteresis behavior of inverse-spinel α-ferrite nanoparticles synthesized by co-precipitation method. Results in physics. 2018;8:93-8.
45. Zhang W, Zuo X, Zhang D, Wu C, Silva SRP. Cr3+ substituted spinel ferrite nanoparticles with high coercivity. Nanotechnology. 2016;27(24):245707.
46. Ashour A, El-Batal AI, Maksoud MA, El-Sayyad GS, Labib S, Abdeltwab E, et al. Antimicrobial activity of metal-substituted cobalt ferrite nanoparticles synthesized by sol–gel technique. Particuology. 2018;40:141-51.
47. Velhal N, Patil N, Shelke A, Deshpande N, Puri V. Structural, dielectric and magnetic properties of nickel substituted cobalt ferrite nanoparticles: Effect of nickel concentration, AIP Adv. 5 (9), 097166 (2015). DOI: https://doi org/101063/14931908. 2015.
48. Vestal CR, Zhang ZJ. Synthesis of CoCrFeO4 nanoparticles using microemulsion methods and size-dependent studies of their magnetic properties. Chemistry of materials. 2002;14(9):3817-22.
49. Özdemir ZG, Kılıç M, Karabul Y, Mısırlıoğlu BS, Çakır Ö, Kahya ND. A transition in the electrical conduction mechanism of CuO/CuFe 2 O 4 nanocomposites. J Electroceram. 2020;44:1-15.
50. Ansari MA, Baykal A, Asiri S, Rehman S. Synthesis and characterization of antibacterial activity of spinel chromium-substituted copper ferrite nanoparticles for biomedical application. Journal of Inorganic and Organometallic Polymers and Materials. 2018;28:2316-27.
51. Bhowmik R. Temperature-and frequency-activated semiconductor-to-metal transition in soft ferromagnetic Li0. 5Mn0. 5Fe2O4 ferrite. Materials Research Express. 2014;1(1):015903.
52. Bhowmik R, Kumar KA. Role of pH value during material synthesis and grain-grain boundary contribution on the observed semiconductor to metal like conductivity transition in Ni1. 5Fe1. 5O4 spinel ferrite. Materials Chemistry and Physics. 2016;177:417-28.
53. Kumar KA, Bhowmik R. Effect of annealing temperatures on the electrical conductivity and dielectric properties of Ni1. 5Fe1. 5O4 spinel ferrite prepared by chemical reaction at different pH values. Materials Research Express. 2017;4(12):126105.
54. Younas M, Nadeem M, Atif M, Grossinger R. Metal-semiconductor transition in NiFe2O4 nanoparticles due to reverse cationic distribution by impedance spectroscopy. Journal of Applied Physics. 2011;109(9).
55. Ata-Allah S, Kaiser M. Semiconductor-to-metallic transition in Cu-substituted Ni–Mn ferrite. physica status solidi (a). 2004;201(14):3157-65.
56. Kannan R, Rajagopan S, Arunkumar A, Vanidha D, Murugaraj R. Unusual metallic behavior in nanostructured cobalt ferrite at superparamagnetic regime. Journal of Applied Physics. 2012;112(6).
57. Bhowmik R, Vijayasri G. Study of microstructure and semiconductor to metallic conductivity transition in solid state sintered Li0. 5Mn0. 5Fe2O4− δ spinel ferrite. Journal of Applied Physics. 2013;114(22).
58. Bhowmik R, Lone AG. Dielectric properties of α-Fe1. 6Ga0. 4O3 oxide: A promising magneto-electric material. Journal of Alloys and Compounds. 2016;680:31-42.

59. Mourdikoudis S, Pallares RM, Thanh NT. Characterization techniques for nanoparticles: comparison and complementarity upon studying nanoparticle properties. Nanoscale. 2018;10(27):12871-934.
60. Inkson BJ. Scanning electron microscopy (SEM) and transmission electron microscopy (TEM) for materials characterization. Materials characterization using nondestructive evaluation (NDE) methods: Elsevier; 2016. p. 17-43.
61. Mehta S, Malik K. Nanoparticles: Preparation, Properties and Applications. Shweta Sharma. 2023:11.
62. Seffati K, Esmaeili H, Honarvar B, Esfandiari N. AC/CuFe2O4@ CaO as a novel nanocatalyst to produce biodiesel from chicken fat. Renewable Energy. 2020;147:25-34.
63. Feyzi M, Hassankhani A, Rafiee HR. Preparation and characterization of Cs/Al/Fe3O4 nanocatalysts for biodiesel production. Energy conversion and management. 2013;71:62-8.
64. Yan Q, Wan C, Liu J, Gao J, Yu F, Zhang J, et al. Iron nanoparticles in situ encapsulated in biochar-based carbon as an effective catalyst for the conversion of biomass-derived syngas to liquid hydrocarbons. Green Chemistry. 2013;15(6):1631-40.
65. Srivastava M, Srivastava N, Mishra PK, Gupta VK. Nanomaterials in biofuels research: Springer; 2020.
66. Gielen D, Boshell F, Saygin D, Bazilian MD, Wagner N, Gorini R. The role of renewable energy in the global energy transformation. Energy strategy reviews. 2019;24:38-50.
67. Newell R, Raimi D, Aldana G. Global energy outlook 2019: the next generation of energy. Resources for the Future. 2019;1(8).
68. Höök M, Tang X. Depletion of fossil fuels and anthropogenic climate change—A review. Energy policy. 2013;52:797-809.
69. Wang J, Feng L, Tang X, Bentley Y, Höök M. The implications of fossil fuel supply constraints on climate change projections: A supply-side analysis. Futures. 2017;86:58-72.
70. Su J, Vayssieres L. A place in the sun for artificial photosynthesis? ACS Energy Letters. 2016;1(1):121-35.
71. Awasthi A, Shukla AK, SR MM, Dondariya C, Shukla K, Porwal D, et al. Review on sun tracking technology in solar PV system. Energy Reports. 2020;6:392-405.
72. Kroposki B, Margolis R, Ton D. Harnessing the sun. IEEE Power and Energy Magazine. 2009;7(3):22-33.
73. Sun Y, Zhao Z, Yang M, Jia D, Pei W, Xu B. Overview of energy storage in renewable energy power fluctuation mitigation. CSEE Journal of Power and Energy Systems. 2019;6(1):160-73.
74. Khaligh A, Li Z. Battery, ultracapacitor, fuel cell, and hybrid energy storage systems for electric, hybrid electric, fuel cell, and plug-in hybrid electric vehicles: State of the art. IEEE transactions on Vehicular Technology. 2010;59(6):2806-14.
75. Barroso LA, Hölzle U. The case for energy-proportional computing. Computer. 2007;40(12):33-7.

76. Lewis NS, Nocera DG. Powering the planet: Chemical challenges in solar energy utilization. Proceedings of the National Academy of Sciences. 2006;103(43):15729-35.
77. Hammarstrom L. Artificial photosynthesis and solar fuels. ACS Publications; 2009. p. 1859-60.
78. El-Khouly ME, El-Mohsnawy E, Fukuzumi S. Solar energy conversion: From natural to artificial photosynthesis. Journal of photochemistry and photobiology C: Photochemistry Reviews. 2017;31:36-83.
79. Gust D, Moore TA, Moore AL. Solar fuels via artificial photosynthesis. Accounts of chemical research. 2009;42(12):1890-8.
80. Stolarczyk JK, Bhattacharyya S, Polavarapu L, Feldmann J. Challenges and prospects in solar water splitting and CO2 reduction with inorganic and hybrid nanostructures. ACS Catalysis. 2018;8(4):3602-35.
81. Corma A, Garcia H. Photocatalytic reduction of CO2 for fuel production: Possibilities and challenges. Journal of Catalysis. 2013;308:168-75.
82. Shehzad N, Tahir M, Johari K, Murugesan T, Hussain M. A critical review on TiO2 based photocatalytic CO2 reduction system: Strategies to improve efficiency. Journal of CO2 Utilization. 2018;26:98-122.
83. Ikreedeegh RR, Tahir M. A critical review in recent developments of metal-organic-frameworks (MOFs) with band engineering alteration for photocatalytic CO2 reduction to solar fuels. Journal of CO2 Utilization. 2021;43:101381.
84. Jeyalakshmi V, Mahalakshmy R, Krishnamurthy K, Viswanathan B, editors. Photocatalytic reduction of carbon dioxide by water: a step towards sustainable fuels and chemicals. Materials Science Forum; 2013: Trans Tech Publ.
85. Durst J, Rudnev A, Dutta A, Fu Y, Herranz J, Kaliginedi V, et al. Electrochemical CO_2 reduction–a critical view on fundamentals, materials and applications. Chimia. 2015;69(12):769-.
86. Centi G, Perathoner S. Towards solar fuels from water and CO2. ChemSusChem: Chemistry & Sustainability Energy & Materials. 2010;3(2):195-208.
87. Li K, Peng B, Peng T. Recent advances in heterogeneous photocatalytic CO2 conversion to solar fuels. Acs Catalysis. 2016;6(11):7485-527.
88. Jia C, Gao J, Dai Y, Zhang J, Yang Y. The thermodynamics analysis and experimental validation for complicated systems in CO2 hydrogenation process. Journal of energy chemistry. 2016;25(6):1027-37.
89. Kumaravel V, Bartlett J, Pillai SC. Photoelectrochemical conversion of carbon dioxide (CO2) into fuels and value-added products. ACS Energy Letters. 2020;5(2):486-519.
90. Lim RJ, Xie M, Sk MA, Lee J-M, Fisher A, Wang X, et al. A review on the electrochemical reduction of CO2 in fuel cells, metal electrodes and molecular catalysts. Catalysis Today. 2014;233:169-80.
91. Gao D, Cai F, Wang G, Bao X. Nanostructured heterogeneous catalysts for electrochemical reduction of CO2. Current Opinion in Green and Sustainable Chemistry. 2017;3:39-44.
92. Zhang W, Hu Y, Ma L, Zhu G, Wang Y, Xue X, et al. Progress and perspective of electrocatalytic CO2 reduction for renewable carbonaceous fuels and chemicals. Advanced Science. 2018;5(1):1700275.

93. Vu NN, Kaliaguine S, Do TO. Critical aspects and recent advances in structural engineering of photocatalysts for sunlight-driven photocatalytic reduction of CO2 into fuels. Advanced Functional Materials. 2019;29(31):1901825.
94. Osterloh FE. Photocatalysis versus photosynthesis: a sensitivity analysis of devices for solar energy conversion and chemical transformations. ACS Energy Letters. 2017;2(2):445-53.
95. Rajeshwar K, Thomas A, Janáky C. Photocatalytic activity of inorganic semiconductor surfaces: myths, hype, and reality. ACS Publications; 2015. p. 139-47.
96. Schneider J, Bahnemann D, Ye J, Puma GL, Dionysiou DD. Photocatalysis: fundamentals and perspectives: Royal Society of Chemistry; 2016.
97. Herrmann J-M. Heterogeneous photocatalysis: fundamentals and applications to the removal of various types of aqueous pollutants. Catalysis today. 1999;53(1):115-29.
98. Li J, Wu N. Semiconductor-based photocatalysts and photoelectrochemical cells for solar fuel generation: a review. Catalysis Science & Technology. 2015;5(3):1360-84.
99. Van Gerven T, Mul G, Moulijn J, Stankiewicz A. A review of intensification of photocatalytic processes. Chemical Engineering and Processing: Process Intensification. 2007;46(9):781-9.
100. Hoffmann MR, Martin ST, Choi W, Bahnemann DW. Environmental applications of semiconductor photocatalysis. Chemical reviews. 1995;95(1):69-96.
101. Kisch H. Semiconductor photocatalysis—mechanistic and synthetic aspects. Angewandte Chemie International Edition. 2013;52(3):812-47.
102. Neaţu Ş, Maciá-Agulló JA, Garcia H. Solar light photocatalytic CO2 reduction: general considerations and selected bench-mark photocatalysts. International journal of molecular sciences. 2014;15(4):5246-62.
103. Fresno F, Villar-García IJ, Collado L, Alfonso-González E, Reñones P, Barawi M, et al. Mechanistic view of the main current issues in photocatalytic CO2 reduction. The journal of physical chemistry letters. 2018;9(24):7192-204.
104. Karim KMR, Ong HR, Abdullah H, Yousuf A, Cheng CK, Khan MMR. Electrochemical study of copper ferrite as a catalyst for CO2 photoelectrochemical reduction. Bulletin of Chemical Reaction Engineering & Catalysis. 2018;13(2):236.
105. Kezzim A, Nasrallah N, Abdi A, Trari M. Visible light induced hydrogen on the novel hetero-system CuFe2O4/TiO2. Energy Conversion and Management. 2011;52(8-9):2800-6.
106. Khan MMR, Uddin MR, Abdullah H, Karim KMR, Yousuf A, Cheng CK, et al. Preparation and characterization of CuFe2O4/TiO2 photocatalyst for the conversion of CO2 into methanol under visible light. International Journal of Chemical and Molecular Engineering. 2016;10(10):1273-80.
107. Sharma S, Jakhar P, Sharma H. CuFe2O4 nanomaterials: Current discoveries in synthesis, catalytic efficiency in coupling reactions, and their environmental applications. Journal of the Chinese Chemical Society. 2023;70(2):107-27.
108. Masunga N, Mmelesi OK, Kefeni KK, Mamba BB. Recent advances in copper ferrite nanoparticles and nanocomposites synthesis, magnetic properties and application in water treatment. Journal of Environmental Chemical Engineering. 2019;7(3):103179.

109. Shetty K, Renuka L, Nagaswarupa H, Nagabhushana H, Anantharaju K, Rangappa D, et al. A comparative study on CuFe2O4, ZnFe2O4 and NiFe2O4: morphology, impedance and photocatalytic studies. Materials Today: Proceedings. 2017;4(11):11806-15.
110. Murugesan S, Balasubramanian S, Perumal E. Copper oxide nanoparticles induced reactive oxygen species generation: A systematic review and meta-analysis. Chemico-Biological Interactions. 2024:111311.
111. Guzman M, Arcos M, Dille J, Rousse C, Godet S, Malet L. Effect of the concentration and the type of dispersant on the synthesis of copper oxide nanoparticles and their potential antimicrobial applications. ACS omega. 2021;6(29):18576-90.
112. Udhaya PA, Ahmad A, Meena M, Queen MAJ, Aravind M, Velusamy P, et al. Copper Ferrite nanoparticles synthesised using a novel green synthesis route: Structural development and photocatalytic activity. Journal of Molecular Structure. 2023;1277:134807.
113. Glazkova E, Bakina O, Rodkevich N, Mosunov A, Vornakova E, Chzhou V, et al. Copper ferrite/copper oxides (I, II) nanoparticles synthesized by electric explosion of wires for high performance photocatalytic and antibacterial applications. Materials Science and Engineering: B. 2022;283:115845.
114. Qin S, Xin F, Liu Y, Yin X, Ma W. Photocatalytic reduction of CO2 in methanol to methyl formate over CuO–TiO2 composite catalysts. Journal of colloid and interface science. 2011;356(1):257-61.
115. Gusain R, Kumar P, Sharma OP, Jain SL, Khatri OP. Reduced graphene oxide–CuO nanocomposites for photocatalytic conversion of CO2 into methanol under visible light irradiation. Applied Catalysis B: Environmental. 2016;181:352-62.
116. Navarro-Jaén S, Virginie M, Bonin J, Robert M, Wojcieszak R, Khodakov AY. Highlights and challenges in the selective reduction of carbon dioxide to methanol. Nature Reviews Chemistry. 2021;5(8):564-79.
117. Thatikayala D, Min B. Copper ferrite supported reduced graphene oxide as cathode materials to enhance microbial electrosynthesis of volatile fatty acids from CO2. Sci Total Environ. 2021;768:144477.
118. Nirumand L, Farhadi S, Zabardasti A, Khataee A. Copper ferrite nanoparticles supported on MIL-101/reduced graphene oxide as an efficient and recyclable sonocatalyst. Journal of the Taiwan Institute of Chemical Engineers. 2018;93:674-85.
119. Talaei M, Hassanzadeh-Tabrizi S, Saffar-Teluri A. Synthesis of mesoporous CuFe2O4@ SiO2 core-shell nanocomposite for simultaneous drug release and hyperthermia applications. Ceramics International. 2021;47(21):30287-97.
120. Naghikhani R, Nabiyouni G, Ghanbari D. Simple and green synthesis of CuFe 2 O 4–CuO nanocomposite using some natural extracts: photo-degradation and magnetic study of nanoparticles. Journal of Materials Science: Materials in Electronics. 2018;29:4689-703.
121. Alshamkhani MT, Putri LK, Lahijani P, Lee KT, Mohamed AR. A metal-free electrochemically exfoliated graphene/graphitic carbon nitride nanocomposite for CO2 photoreduction to methane under visible light irradiation. Journal of Environmental Chemical Engineering. 2023;11(1):109086.

122. Goyal S, Shaharun MS, Kait CF, Abdullah B, Ameen M. Photoreduction of carbon dioxide to methanol over copper based zeolitic imidazolate framework-8: a new generation photocatalyst. Catalysts. 2018;8(12):581.
123. Thompson WA, Sanchez Fernandez E, Maroto-Valer MM. Review and analysis of CO2 photoreduction kinetics. ACS Sustainable Chemistry & Engineering. 2020;8(12):4677-92.
124. Mohammed A. Alzahran F, Arshad J, Al-Buriahi M, Alrowaili Z, Munir S. Synthesis of graphene-based Ag-doped CuFe2O4 composite for improved photocatalytic activity against industrial effluents. Journal of Taibah University for Science. 2023;17(1):2209676.
125. Jillani S, Jelani M, Hassan NU, Ahmad S, Hafeez M. Synthesis, characterization and biological studies of copper oxide nanostructures. Materials Research Express. 2018;5(4):045006.
126. Varghese D, S. R N, P JSJ, S M. Synergistic design of CuO/$CoFe_2O_4$/MWCNTs ternary nanocomposite for enhanced photocatalytic degradation of tetracycline under visible light. Scientific Reports. 2025;15(1):320.
127. Khan MMR, Uddin MR, Abdullah H, Karim KMR, Yousuf A, Cheng CK, et al. Preparation and characterization of CuFe2O4/TiO2 photocatalyst for the conversion of CO2 into methanol under visible light. International journal of chemical, molecular, nuclear, materials and metallurgical engineering. 2016;10:1165-72.
128. Karim KMR, Tarek M, Sarkar SM, Mouras R, Ong HR, Abdullah H, et al. Photoelectrocatalytic reduction of CO2 to methanol over CuFe2O4@ PANI photocathode. Int J Hydrogen Energy. 2021;46(48):24709-20.
129. Elemike EE, Onwudiwe DC, Singh M. Eco-friendly synthesis of copper oxide, zinc oxide and copper oxide–zinc oxide nanocomposites, and their anticancer applications. Journal of Inorganic and Organometallic Polymers and Materials. 2020;30(2):400-9.
130. El-Masry MM, El-Shahat M, Ramadan R, Abdelhameed RM. Selective photocatalytic reduction of nitroarenes into amines based on cobalt/copper ferrite and cobalt-doped copper ferrite nano-photocatalyst. Journal of Materials Science: Materials in Electronics. 2021;32(13):18408-24.
131. Shafiey Dehaj M, Zamani Mohiabadi M. Experimental study of water-based CuO nanofluid flow in heat pipe solar collector. J Therm Anal Calorim. 2019;137:2061-72.
132. Yadav VK, Ali D, Khan SH, Gnanamoorthy G, Choudhary N, Yadav KK, et al. Synthesis and characterization of amorphous iron oxide nanoparticles by the sonochemical method and their application for the remediation of heavy metals from wastewater. Nanomaterials. 2020;10(8):1551.
133. Massoud-Sharifi A, Kara GK, Rabbani M, editors. CuFe2O4@ CuO: a magnetic composite synthesized by ultrasound irradiation and degradation of methylene blue on its surface in the presence of sunlight. Proceedings; 2019: MDPI.
134. Wang J, Deng Q, Li M, Jiang K, Zhang J, Hu Z, et al. Copper ferrites@ reduced graphene oxide anode materials for advanced lithium storage applications. Scientific reports. 2017;7(1):8903.

135. Salavati-Niasari M, Mahmoudi T, Sabet M, Hosseinpour-Mashkani SM, Soofivand F, Tavakoli F. Synthesis and characterization of copper ferrite nanocrystals via coprecipitation. J Cluster Sci. 2012;23:1003-10.
136. Rani BJ, Saravanakumar B, Ravi G, Ganesh V, Ravichandran S, Yuvakkumar R. Structural, optical and magnetic properties of CuFe 2 O 4 nanoparticles. Journal of Materials Science: Materials in Electronics. 2018;29:1975-84.
137. Chandrappa K, Venkatesha T. Generation of nanostructured CuO by electrochemical method and its Zn–Ni–CuO composite thin films for corrosion protection. Mater Corros. 2013;64(9):831-9.
138. Zhang Y, Yao D, Xia B, Jaroniec M, Ran J, Qiao S-Z. Photocatalytic CO2 reduction: identification and elimination of false-positive results. ACS Energy Letters. 2022;7(5):1611-7.
139. Liu Y, Ge Q, Wang T, Li K, Deng Y, You W, et al. Investigating the impact of pretreatment strategies on photocatalyst for accurate CO2RR productivity quantification: a machine learning approach. Chem Eng J. 2023;473:145255.
140. Goyal S, Shaharun MS, Kait CF, Abdullah B, editors. Effect of monometallic copper on zeolitic imidazolate framework-8 synthesized by hydrothermal method. Journal of Physics: Conference Series; 2018: IOP Publishing.
141. Thompson W, Fernandez ES, Maroto-Valer M. Probability Langmuir-Hinshelwood based CO2 photoreduction kinetic models. Chem Eng J. 2020;384:123356.
142. Tan L-L, Ong W-J, Chai S-P, Mohamed AR. Photocatalytic reduction of CO2 with H2O over graphene oxide-supported oxygen-rich TiO2 hybrid photocatalyst under visible light irradiation: Process and kinetic studies. Chem Eng J. 2017;308:248-55.
143. Seeharaj P, Kongmun P, Paiplod P, Prakobmit S, Sriwong C, Kim-Lohsoontorn P, et al. Ultrasonically-assisted surface modified TiO2/rGO/CeO2 heterojunction photocatalysts for conversion of CO2 to methanol and ethanol. Ultrason Sonochem. 2019;58:104657.